Phase matrix characterization of long-range transported Saharan dust using multiwavelength polarized polar imaging nephelometry

Elena Bazo[1,2], Daniel Pérez-Ramírez[1,2], Antonio Valenzuela[1,2], J. Vanderlei Martins[3], Gloria Titos[1,2], Alberto Cazorla[1,2], Fernando Rejano[1,4], Diego Patrón[1,2], Arlett Díaz-Zurita[1,2], Francisco José García-Izquierdo[5], David Fuertes[4], Lucas Alados-Arboledas[1,2] and Francisco José Olmo[1,2]

[1]Andalusian Institute for Earth System Research (IISTA-CEAMA), Granada 18006, Spain

[2]Department of Applied Physics, University of Granada, Granada 18071, Spain

[3]JDepartment of Physics and Earth and Space Institute, University of Maryland, Baltimore County, Baltimore, Maryland, USA

[4]GRASP-SAS, Remote Sensing Developments, Lille, France

[5]Instituto de Astrofísica de Andalucía (IAA-CSIC), Granada 18008

Correspondence to: Daniel Pérez-Ramírez (dperez@ugr.es)

Abstract. This work investigates the scattering matrix elements during different Saharan dust outbreaks over Granada (South-East Spain) in 2022 using a Polarized Imaging Nephelometer (PI-Neph) capable of measuring continuously the phase function (F_{11}) and the polarized phase function ($-F_{12}/F_{11}$) at three different wavelengths (405, 515 and 660 nm) in the range 5° - 175°. The focus is in two extreme dust events (PM_{10} > 1000 μgm^{-3}) in March 2022. During the peaks of these events F_{11} and $-F_{12}/F_{11}$ show the classical patterns observed for dust samples in laboratory measurements available in the Amsterdam-Granada Light Scattering database at all wavelengths. However, for the moments prior and after the peaks the results reveal important sensitivity in $-F_{12}/F_{11}$ at 405 nm. For the other wavelengths, however, this difference in $-F_{12}/F_{11}$ is not evident. Moreover, no remarkable changes are found in F_{11} that is always characterized by strong predominance of forward scattering. The analyses of more frequent and moderate events registered in summer 2022 (PM_{10} between 50 and 100 μgm^{-3}) revealed F_{11} and $-F_{12}/F_{11}$ patterns like those observed prior and after the extreme events. The combination of PI-Neph measurements with additional in-situ instrumentation allowed a typing classification that revealed the peaks in the extreme dust events as pure dust, while for the rest of cases remarked a mixture of dust with urban background pollution. In addition, simulations with the Generalized Retrieval of Atmosphere and Surface Properties (GRASP) code explain the different patterns in $-F_{12}/F_{11}$ with changes in the refractive indexes and with the different contributions of the fine and coarse mode.

1 Introduction

The imprecise determination of atmospheric aerosol microphysical properties is currently the main source of uncertainty in climate projections, as stated by the latest Intergovernmental Panel on Climate Change (IPCC – Forster et al., (2021)). Particularly, aerosol particles can scatter and absorb solar radiation, known as the direct effect (Haywood et al., 2000). Moreover, aerosol particles can interact with clouds in different ways: aerosol absorption can modify the energy balance in the atmosphere affecting cloud development and properties (the semi-direct effect – Fan et al., (2016)). They can also serve as cloud condensation nuclei (CCN) and ice nucleating particles (INP) upon which cloud droplets and ice crystals form (the aerosol indirect effect on clouds – Rosenfeld et al., (2014)).

Advancing in aerosol knowledge faces complex challenges due to the large variability of aerosol types and to aerosol sources and transformation processes in the atmosphere during their transport. More specifically, mineral dust is the most important source of primary particles in the atmosphere with an estimated emission rate of 1000-3000 Tg/year representing about half of the annual particle mass emission at the global scale (Kok et al., 2021). Mineral dust sources extend over a wide area on the planet highlighting the global dust belt that extends from the arid regions of the west coast of northern Africa through the Middle East and Central Asia. Such a belt includes the Sahara Desert, which is the largest in the world being responsible for almost 50% of the global dust emissions (Kok et al., 2017). In this sense, recent studies (Kok et al., 2018) estimate the direct dust-climate feedback parameter associated with the direct radiative effect in the range -0.04 to + 0.02 $Wm^{-2}°C^{-1}$ (net, short + long wavelength), but being highly dependent on the model used. The problem with understanding the role of dust in climate becomes even more complex due to the changes in arid lands since the pre-industrial era, which is producing an increase of global dust mass loading (Kok et al., 2017). Most of these uncertainties are due to the challenges in better understanding mineral dust composition and variability with size and sources (Gonçalves Ageitos et al., 2023).

Mineral dust particles are typically considered as large particles in the coarse (1-10 µm) and super-coarse (> 10 µm) modes (J. B. Renard et al., 2018), although recent studies have also shown the presence of a fine mode (ranges below 1 µm diameter) in mineral dust (Huang et al., 2019). The current discrepancies about the roles of fine, coarse and super-coarse modes in the dust sample (González-Flórez et al., 2023) imply difficulties in dust modelling that add uncertainties to the climate modelling (A. A. Adebiyi & Kok, 2020). One critical point is the modelling of coarse mode because of the non-sphericity of these types of particles (Mishchenko et al., 2002), and also inferring the complex refractive index (Formenti et al., 2003) that ultimately depends on particle size, shape and chemical composition (González-Romero et al., 2023). For example, iron oxides are the key to understanding the mineral dust absorption properties in the UV (e.g. hematite, goethite) whilst Ca-rich carbonates become important in the infrared region (Formenti et al., 2014). These variabilities in size-related and absorption parameters difficult modelling accurately the response of mineral dust to direct radiative effect (A. Adebiyi et al., 2023). The problem becomes even more complex because the interactions of dust particles with other precursor gases and aerosol particles already presented in the atmosphere (Ooki & Uematsu, 2005). For example, the variabilities in dust size, shape and chemical composition are also related to emerging questions such as the role of big mineral dust particles in new particle formation in the atmosphere (Casquero-Vera et al., 2023).

Remote sensing techniques are widely used to infer dust properties. For example, passive remote sensing techniques such as sun-photometry by the Aerosol Robotic Network (AERONET – (Holben et al., 1998)) or star/moon photometry (i.e Pérez-Ramírez et al., 2008, Pérez-Ramírez et al., 2011;Berkoff et al., 2011) allow to have a representation of column-integrated values, particularly aerosol optical depth (AOD). But to infer other aerosol optical (e.g. aerosol complex refractive index and single scattering albedo) and microphysical (e.g. aerosol size distribution) properties it is necessary to solve ill-posed problems where the information content is low (Dubovik & King, 2000; King et al., 1978; Nakajima et al., 1996; Olmo et al., 2006, 2008; Pérez-Ramírez et al., 2015). These algorithms use the Mie theory for the internal computation of particles phase functions, but in the case of dust particles more complex approaches such as T-Matrix are needed because of the non-sphericity of dust particles (Mischenko & Travis, 1994, 1997) . Nevertheless, several inversion algorithms have been developed incorporating T-Matrix modeling, being one of the most popular algorithms developed within the AERONET network (Dubovik et al., 2006).

Ground-based remote sensing techniques are only representative of the measurement site, and to face these limitations satellite measurements are ideal because they can cover wide regions of the world. However, passive remote sensing space platforms deal with additional complexity in the retrieval of aerosol properties because of the influence of surface reflectance (Kahn et al., 1998; Levy et al., 2007). The simplest retrievals use look-up tables with a priori aerosol types with great success in obtaining AOD, but limited capacity for obtaining other aerosol parameters because of the difficulties to separate the signals corresponding to the atmosphere and surface (Dubovik et al., 2019). To solve these limitations, the use of multiwavelength and multi-angle polarization measurements is ideal to improve the information content (Mishchenko et al., 2007). Some of the first polarized-based measurements for aerosol studies were carried out by the POLDER instrument (POlarization and Directionality of the Earth's Reflectances – (Deuzé et al., 1993)) that acquired 9 years of data. These measurements were used as inputs in the Generalized Retrieval of Atmosphere and Surface Properties algorithm (GRASP –(Dubovik et al., 2014, 2021)) for obtaining extended aerosol optical and microphysical properties. Algorithms such as GRASP are becoming the operational algorithms in new satellite missions (Remer et al., 2019; Fuertes et al., 2022; Hasekamp et al., 2024), but these algorithms need phase matrix measurements that allow to optimize the kernels used internally, particularly for non-spherical particles.

The main difficulties lie in measuring aerosol phase matrix of ambient air are in the design and development of appropriate polar nephelometry capable of measuring light scattered with appropriate angular resolution. The first polar nephelometry developments were based on moveable detectors, but they must be mechanically stable and require a constant population of aerosol particles that does not change appreciably during the detector sweep (Holland & Gagne, n.d.; Hovenier et al., 2003; Jaggard et al., 1981; Kuik et al., 1991; Perry et al., 1978; Volten et al., 2001a). Other polar nephelometry designs use arrays of many detectors placed on representative scattering angles (Barkey et al., 1999; Gayet et al., 1998; Pope et al., 1992; West et al., 1997; Wyatt et al., 1988), but this technique requires careful calibration of the detectors and generally suffers from low angular resolution (~2º). Those instrumental limitations have implied that the usual study of scattering matrix elements of dust particles is done in the laboratory for synthetic samples minerals that compose dust particles (Curtis et al., 2008; Huang et al., 2020; Meland et al., 2010; Muñoz et al., 2010a; J. B. Renard et al., 2014; J.-B. Renard et al., 2010) or with collected dust samples (Muñoz et al., 2007a; J. B. Renard et al., 2014; J.-B. Renard et al., 2010, 2024). Actually, the parametrizations of mineral dust phase matrix used for AERONET algorithm were calculated by fitting the laboratory measurements of different non-spherical particles samples (i.e. Dubovik et al., 2006). Such measurements were performed at a few wavelengths, and what is more important, they might be non-representative of real aerosol measurements because of the different transformations and interactions of dust particles since they were emitted in their source regions. There is therefore a current challenge in having an extended database of measurements of dust phase matrix elements for different dust types and mixtures, particularly at different stages of dust evolution after their emission from the remote desert areas.

The latest developments use imaging techniques (Bian et al., 2017; Curtis et al., 2007; Dolgos & Martins, 2014) to determine phase matrix with single detector and relatively compact design that does not require moveable parts. The Polarized Imaging Nephelometer (PI-Neph) was one of the first designs of a polar nephelometer that used imaging techniques, developed by the University of Maryland, Baltimore County (UMBC). This first prototype of the PI-Neph could acquire aerosol phase matrix at 473, 532 and 671 nm with 0.5º resolution. The instrument was deployed on the NASA DC8 aircraft and operated during special field (Espinosa et al., 2018; Reed Espinosa et al., 2017). Other PI-Neph instruments based on the first UMBC design are operated by NOAA (Ahern et al., 2022; Manfred et al., 2018). The main novelty of these prototypes is that they measure phase matrix elements of ambient air, where conditions can be very different to laboratory measurements. However, to date none of these instruments have been operating continuously and reported any multiwavelength measurements of Saharan dust. The imaging technique is being expanded worldwide with further designs although limited to laboratory operation yet (Moallemi et al., 2023). All designs in polar nephelometry present physical limitations that limit the measurements to the range 3º-178º, but synthetic tests have revealed that multi-wavelength polarimetric PI-Neph measurements improve the information content for the retrieval of aerosol optical and microphysical properties (Moallemi et al., 2022) . Therefore, measurements of dust phase matrix elements for ambient aerosol samples in the atmosphere will serve to advance in the understanding of mineral dust absorption properties and chemical composition (Di Biagio et al., 2017, 2019).

This work presents phase matrix measurements of ambient Saharan dust particles by the GRASP-Earth's (https://www.grasp-earth.com/) multi-wavelength PI-Neph. The instrument was developed using the heritage of previous PI-Neph developments made by UMBC and can provide aerosol phase matrix elements at 405, 515 and 660 nm of ambient samples in the range 5° - 175° with 1° resolution. Measurements were acquired in the urban background station (UGR) of the Andalusian Global ObseRvatory of the Atmosphere (AGORA) located in the Southeast of the Iberian Peninsula where the main source of natural particles is the Sahara Desert's transported particles (Querol et al., 2019). We present the results for extreme outbreaks that occurred in March 2022 (Rodríguez & López-Darias, 2024) with PM_{10} (particulate matter with diameter < 10 µm) concentrations over 1000 μgm^{-3}, and for more typical situations of moderate dust events with PM_{10} concentrations around 100 μgm^{-3}. The measurements presented of the phase matrix for Saharan dust are unique and are and step forward from the ancillary measurements performed in the region by Horvath et al., (2018) with a single wavelength polar nephelometry (no polarization was available).

This work is structured as follows: in Section 2 we describe the experimental station and the instrumentation, Section 3 gives an overview of the extreme dust events, Section 4 analyzes the results of the optical properties during different dust events, in Section 5 we discuss the results obtained and Section 6 is devoted to the main conclusions and keys for future work.

2 Experimental station and Instrumentation

2.1 Experimental station

Experimental measurements were carried out at the UGR station of the AGORA Observatory in the city of Granada (37.18°N, 3.58°W, 680 m asl) in Southern Spain. The main local source of aerosol particles in the UGR station is road traffic (Titos et al., 2014, 2017), with sporadic presence of biomass burning aerosol (Casquero-Vera et al., 2021; Titos et al., 2017). Air-mass stagnation also favors the accumulation of pollution (Lyamani et al., 2012; Patrón et al., 2017). The city is located 200 km away from the African continent, so long-range transport of Saharan dust to the UGR station is quite common (Lyamani et al., 2010b; Valenzuela et al., 2012a, 2012b). These dust intrusions have mean aerosol optical depths (AOD) of 0.25 ± 0.12 (Pérez-Ramírez et al., 2016) and PM_{10} concentrations ranging between 25 and 200 $\mu g m^{-3}$ (Párraga et al., 2021), although extreme Saharan dust events with AOD above 1.0 also affect the station (Guerrero-Rascado et al., 2009). Most of these intrusions typically occur in summer but in the last years they are becoming more frequent during the winter season (Cazorla et al., 2017; Cuevas-Agulló et al., 2024; Fernández et al., 2019; Titos et al., 2017).

In this study, particles were sampled using a total inlet (no size cut) that consist of a 5 m long stainless-steel tube with a 20 cm diameter (Lyamani et al., 2008). Inside the stainless-steel tube there are several pipes that split the aerosol flow into the different instruments. The inlet system is completely vertical to minimize deposition losses. The final connection to the instruments is performed with conductive tubing avoiding bends. Additionally, all the measurements were at ambient conditions (no aerosol dryer was used). Given the flowrate used in the measurements we can assume that particles are randomly oriented, avoiding the limitations in polarization results of super-coarse particles with particle speed that can orient the particle in particular orientations (Daugeron et al., 2006).

2.2 Instrumentation

2.2.1 Polarized Imaging Nephelometer (PI-Neph)

The PI-Neph (GRASP-Earth PIN-100) is used to obtain direct measurements of two aerosol phase matrix elements, the phase function (F_{11}) and the polarized phase function ($-F_{12}/F_{11}$), at three different wavelengths (405, 515 and 660 nm). The instrument uses previous heritage in PI-Neph developments in the University of Maryland, Baltimore County (Dolgos and Martins, 2014), where the novelty in the PIN-100 is the use of one beam instead of a mirror system to fold the laser beam, as was in previous models. This feature minimizes internal reflection and loss of energy within the laser beam and guarantees that all points along the laser beam will have the same scattering plane orientation, assuring the optimal input polarization state at all scattering angles simultaneously. The optical system counts with a wire grid polarizer and two liquid crystal retarders (LCVRs) that control the state of linear polarization. In this sense, polarized light (parallel or perpendicular) reaches the sample chamber. The light scattered by the aerosol particles is recorded with a 185° field of view CMOS camera, giving the scattered light by the particles in the sample chamber in the range 5°-175°, with 1° angular resolution. More details of the instrument are in Bazo et al., (2024).

An extensive analysis of the error sources in the PI-Neph was performed in Bazo et al., (2024) but an overview is given here: an exhaustive calibration of the instrument is performed consisting of two different steps. The first is a geometric correction that corrects from the different light paths to the different pixels in the CMOS camera. Later the absolute calibration permits to obtain phase matrix elements in physical units. In each step we used known scatterers (CO_2 and particle free air) whose parallel and perpendicular signals can be computed analytically using the Rayleigh theory (Anderson et al., 1996). Evaluation of the calibration with time did reveal great stability (variations around 3%). Instrument stability was evaluated with CO_2 measurements at a constant flow rate of 10 $L min^{-1}$ during 15 min. These measurements revealed constant values of scattering coefficients with differences below 1% versus theoretical values from (Bodhaine et al., 1991). Finally, inherent aspects of the imaging technique were evaluated such as the impact of the exposure time. The largest noise is found for exposure times below 5 s, while the smoother values are obtained for exposure times of 10-20 s. However, large exposure times can yield to more angles that are saturated, and the software must find a compromise between noise and saturation. Thus, the typical exposure time is of 10 s and with that we estimate that uncertainties in measured parallel and perpendicular signals are around 5% in laboratory conditions. The evaluation of the instrument versus known scattered (monodisperse polystyrene spheres - PSL) showed good agreements, being the RMSE around 0.10 for both F_{11} and $-F_{12}/F_{11}$.

The uncertainties in direct measurements of the instrument (parallel and perpendicular signals) are 5% that imply uncertainties below 10% in F_{11} and below 20% in $-F_{12}/F_{11}$. However, in-situ measurements present natural variability of the aerosol sampled and the differences can be enhanced because of the short exposure times (~ 10s). Effects during the measurements such as saturation or low signal to noise ratios (SNR) of some pixels can happen. Other issues such as the passage of an individual super-coarse particle can have an impact on certain angles of the phase matrix. Therefore, we apply a data-quality check procedure that accounts for all these issues and provide an effective phase matrix representative of an average time of 30 min or 1 hour, depending on the specific conditions of natural aerosol variability. Note that standard deviations during these periods might be larger than the uncertainties of the instrument. Details of this quality check procedure are in Bazo et al., (2024).

The direct measurements of F_{11} and $-F_{12}/F_{11}$ with the PI-Neph allow to obtain other aerosol optical parameters such as the scattering coefficient (σ), the asymmetry parameter (g) and the fraction of backscattered light (Bs) using the following equations (Horvath et al., 2018):

$$\sigma_{sca}(\lambda) = \frac{1}{2}\int_0^{180} F_{11}(\theta,\lambda) sin\,\theta \cdot d\theta\ , \qquad (1)$$

$$P_{11}(\theta,\lambda) = \frac{F_{11}(\theta,\lambda)}{\sigma_{sca}(\lambda)}\ , \qquad (2)$$

$$g(\lambda)\ =\ \int_0^{\pi} P_{11}(\theta,\lambda)\cdot\sin\theta\cdot\cos\theta\cdot d\theta\ , \qquad (3)$$

$$B_s(\lambda) = \frac{1}{2}\int_{\frac{\pi}{2}}^{\pi} P_{11}(\theta,\lambda)\cdot\sin\theta\cdot d\theta\ , \qquad (4)$$

where data from 0 to 5° and from 175 to 180° have been linearly extrapolated to obtain the complete phase function. Stepwise extrapolations might be more consistent (i.e. Horvath, 2015), but our additional computations remarked that differences between linear and stepwise extrapolations were below 1% for σ_{sca}, g and B_s. For particle sizes above 4 µm the uncertainties can yield 5% (Horvath, 2015).

2.2.2 Additional in-situ instrumentation at AGORA

AGORA operates other in-situ instruments within the Aerosols, Clouds and Trace gases Research Infrastructure (ACTRIS; https://www.actris.eu/). The integrating nephelometer (TSI model 3563) was used to measure the aerosol particle light scattering coefficient (σ_{sca}) at 450, 550 and 700 nm with a flow rate of 15 $Lmin^{-1}$ and a time resolution of 1 minute. As with the PI-Neph, the integrating nephelometer is calibrated with particle free air and CO_2 and Rayleigh subtraction is applied to measure particle scattering only. Due to experimental limitations the scattered light at the complete forward (0°) and backward (180°) regions cannot be detected, so the angular range for integration is 7-170°. However, results used in this work have been corrected to the entire angular range with the correction proposed by Anderson & Ogren, (1998). On the other hand, we also used the multiwavelength aethalometer (AE33, Magee Scientific) that measures aerosol light absorption coefficient (σ_{abs}) at seven different wavelengths (370, 470, 520, 590, 660, 880 and 950 nm) with a flow rate of 4 $Lmin^{-1}$ and a time resolution of 1 minute. Equivalent black carbon (eBC) concentration is inferred by measuring the absorption coefficient at 880 nm using a mass absorption cross section of 7.77 m^2g^{-1} (Titos et al., 2017). Measurements of the absorption coefficient by the aethalometer are corrected with the one measured by the Multi Angle Absorption Photometer (MAAP, model 5012, Thermo Fisher) at 637 nm. More details of the instruments are in Drinovec et al., (2015) and Petzold and Schönlinner, (2004), respectively.

The scattering and absorption coefficients measured by the integrating nephelometer and the aethalometer, respectively, have been used to calculate the scattering Ångström Exponent (SAE) and the absorption Ångström Exponent (AAE):

$$SAE_{\lambda_1-\lambda_2} = -\frac{\ln\left(\frac{\sigma_{sca}(\lambda_1)}{\sigma_{sca}(\lambda_2)}\right)}{\ln\left(\frac{\lambda_1}{\lambda_2}\right)}\ , \qquad (5)$$

$$AAE_{\lambda_1-\lambda_2} = -\frac{\ln\left(\frac{\sigma_{abs}(\lambda_1)}{\sigma_{abs}(\lambda_2)}\right)}{\ln\left(\frac{\lambda_1}{\lambda_2}\right)} . \tag{6}$$

The wavelengths used in this work to calculate both SAE and AAE have been 405-660 nm and 450-700 nm, respectively. Moreover, measurements of σ_{abs} combined with those of σ_{sca} permit the computation of the extinction coefficient σ_{ext} = σ_{abs}+σ_{sca} and thus obtaining aerosol single scattering albedo (SSA) as:

$$SSA = \frac{\sigma_{sca}}{\sigma_{ext}} , \tag{7}$$

where the Ångström law is used to calculate σ_{abs} for the PI-Neph wavelengths. On the other hand, if $F_{11}(180°)$ is computed the extinction-to-backscattering ratio, widely known as lidar ratio (LRs) in the lidar community, can be computed as:

$$LR = \frac{\sigma_{ext}}{F_{11}(180°)} , \tag{8}$$

The computation of $F_{11}(180°)$ has been made using the interpolation method used for completing the entire angular range in σ_{sca}. Other more robust methods can be used (i.e. Gomez-Martin et al., 2021), that can imply differences in $F_{11}(180°)$ of up to 20-30%. Therefore, LRs estimations will serve as an illustration of how this parameter varies under different conditions. We highlight that PI-Neph is not designed to accurately measure $F_{11}(180º)$ and there are other specific instruments that serve for that purpose (Järvinen et al., 2016; Miffre et al., 2023; Sakai et al., 2010).

3 Overview of extreme dust events during March 2022

During March 2022 the Iberian Peninsula, and particularly its southeast region, was affected by two intense Saharan dust outbreaks, especially during the 15th - 16th and the 24th - 25th of March. Figure 1 shows the geopotential height maps at 850 mb for 15th March 18:00 UTC and 25th March 12:00 UTC, which are close to the peaks of the event in each case. Data shown are from the NCEP/NCAR model (Kalnay et al., 1996; Kanamitsu et al., 2002) – https://tropic.ssec.wisc.edu/archive). On 15th March, Fig. 1a indicates the low-pressure system centered in the southwest of the Iberian Peninsula and northern Morocco associated with low values of geopotential heights. A high-pressure system is present in the central Mediterranean associated with high values of geopotential height. This high-pressure system covers wide regions from central Europe to the Sahara Desert in Libya and Tunisia. The interaction between these low-pressure and high-pressure systems favors strong southeastern winds to the south of the Iberian Peninsula. On 25th March, Fig. 1 reveals very similar patterns, although the low-pressure system is less intense (more sparse lines) and is displaced a little bit towards the east, centered over northern Morocco.

The synoptic situations on the 15th and the 25th of March described in Fig. 1 implied the advection of hot and dry air from the Sahara Desert region in Argelia and southern Morocco. The low-pressure system favored wind gusts and thus the injection of dust particles in the atmosphere, which are later transported long distances by the low-pressure system. This is one of the classical transport patterns of Saharan dust to the Iberian Peninsula (Escudero et al., 2005; Rodríguez et al., 2001; Salvador et al., 2014).

Figures 2 and 3 show total aerosol optical depth (AOD) at 550 nm generated by the CAMS model (Benedetti et al., 2009; Morcrette et al., 2009) over Europe. The wind field at the surface is also represented in these Figures, and different times selected serve to understand how the dust was transported and affected different regions. Figure 2 clearly shows the counterclockwise winds associated with the low-pressure system and how this hot and dry air enters through the southeast reaching the north of the Iberian Peninsula and southern France. That airmass also transports large amounts of mineral dust particles as can be observed by the high values of simulated AODs. It is observed that the largest intensity of dust particles in the southeast of the Iberian Peninsula happened on the evening of 15th March. The wind pattern reveals how dust enters through the southeast of the Iberian Peninsula reaching later the northwest latitudes. The weak wind pattern in the North of the Iberian Peninsula favors the transport to southern France. For the 25th of March (Figure 3), the wind pattern is very similar to that on 15th March (Figure 2), although it does not reach the same northern locations. Indeed, the low-level system configuration seems to facilitate the transport of this hot and dry air to western locations in Portugal and the Atlantic Ocean. The CAMs model also predicts a larger amount of dust particles as indicated by the high AODs.

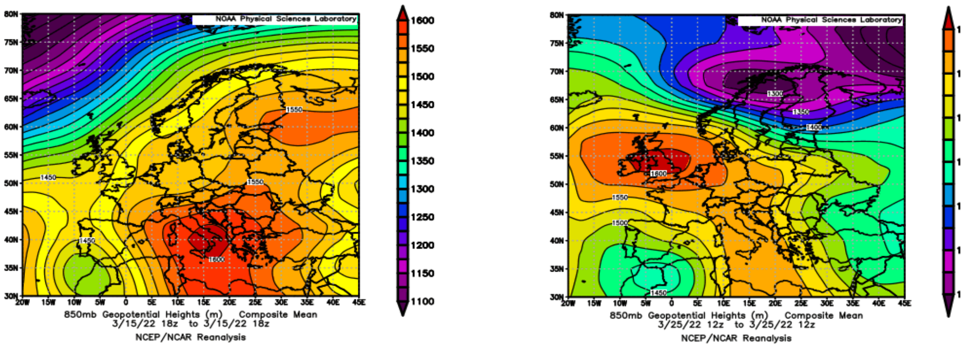

Figure 1: Geopotential height at 850 mb for a) 15th March 2022 at 18:00 UTC and (b) 25th March 2022 at 12:00 UTC. Data are from NCEP/NCAR - https://tropic.ssec.wisc.edu/archive.

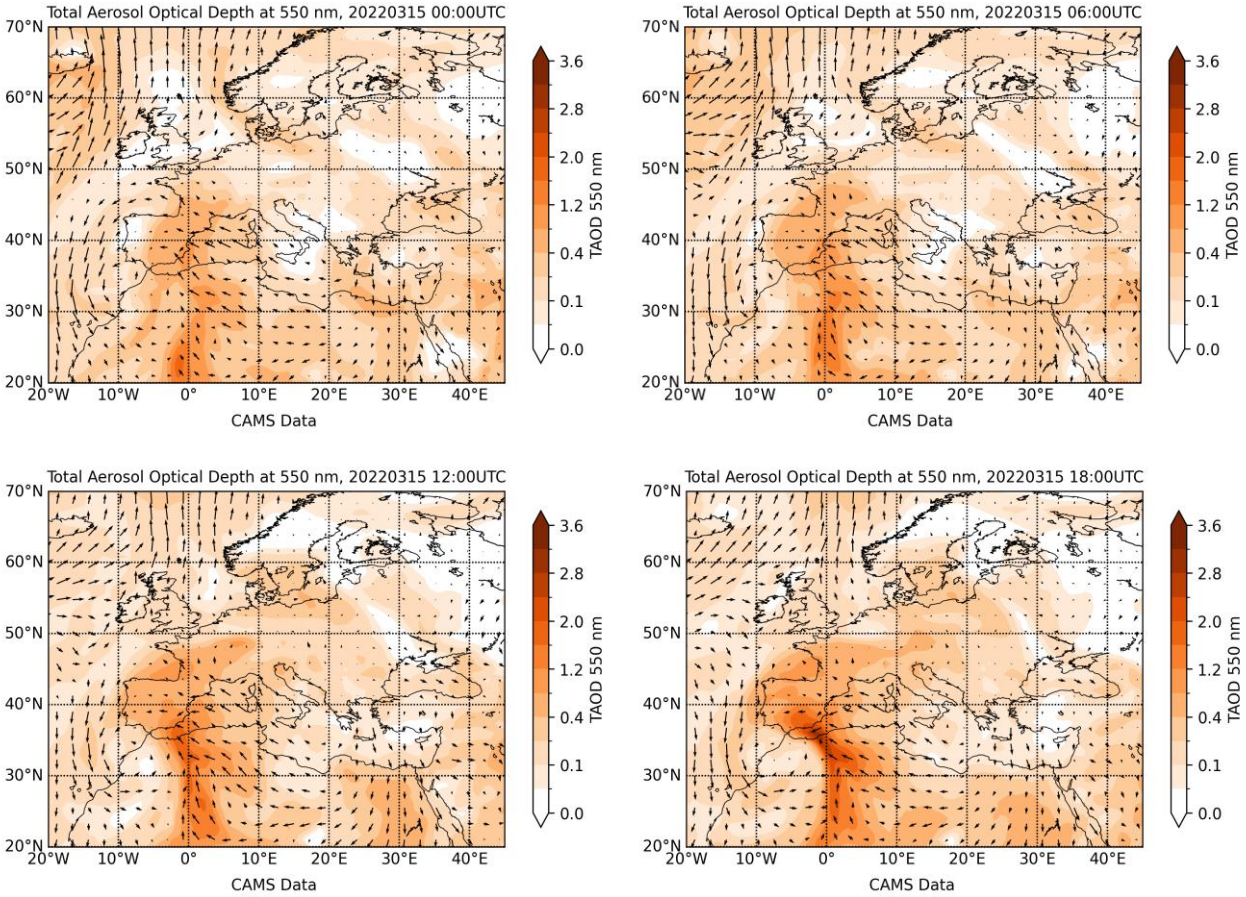

Figure 2: CAMS model simulations of total aerosol optical depth (TAOD) and wind field for different times on 15th March 2022.

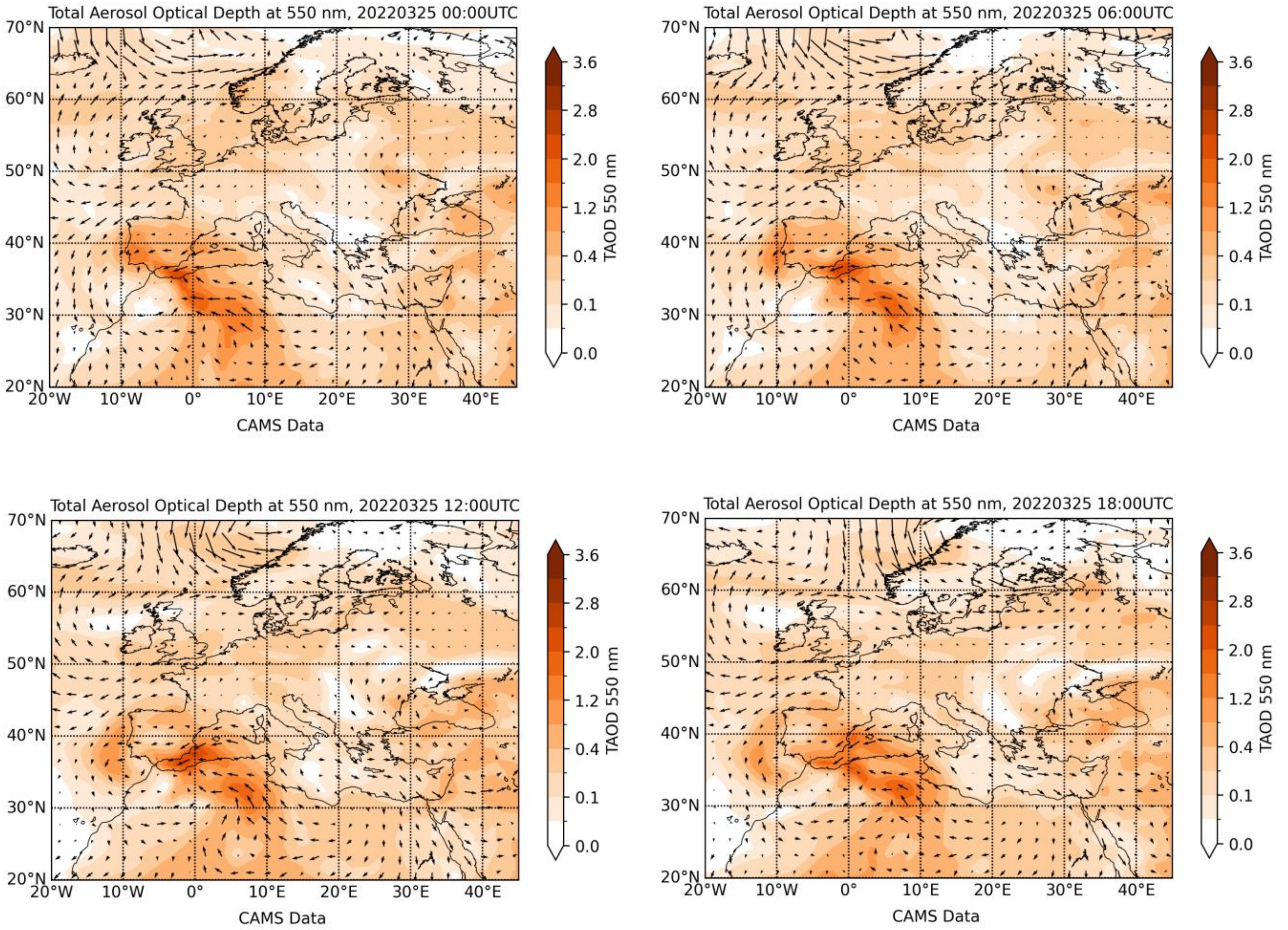

Figure 3: CAMS model simulations of total aerosol optical depth (TAOD) and wind field for different times on 25th March 2022.

Figure 4 shows satellite images provided by NASA worldview (https://wvs.earthdata.nasa.gov) that allow to have a visualization of the intensity of the dust outbreaks over the Iberian Peninsula. On both days, there were presence of clouds in the Iberian Peninsula because of the advection of humidity from the Atlantic by the low-pressure system (more intense on 25th which explains that almost all the Iberian Peninsula was covered by clouds). The image for 15th March clearly shows high presence of dust in the north of the Iberian Peninsula, the Cantabrian Sea and southern France. For the 25th of March the cloud cover hinders dust visualization, but it is observed in the Atlantic in the region between the Canary and Madeira islands. We highlight that such extreme events are not typical in winter season in the Iberian Peninsula, although it is not the first time that similar dust events have been registered in this season (Cazorla et al., 2017; Fernandez et al., 2019; Titos et al., 2017).

The events on 15th and 25th March 2022 can be considered as extreme Saharan dust outbreaks because of the large area covered, but especially because of the large amount of mineral dust particles transported. A more in-depth analysis of satellite images revealed that for the cloud-free pixel registered AODs were between 1.9 - 2.5 on 15th March and between 0.3 – 1.5 on 25th March, which are very high for these locations. The extremely high AODs values on 15th March associated with dust particles were confirmed by AERONET observations with AODs above 1.0 for the stations in northern Spain (A Coruña and Palencia) and southern France (Aubiere, Agen, Archaon and Momuy) where data of Level 2.0 Version 3 are available – graphs not shown for clarity but can be visualized in AERONET webpage (https://aeronet.gsfc.nasa.gov/). These high value of AODs agrees with those reported by CAMS model in Figure 2 and 3. Unfortunately, there is no AERONET data Level 2.0 Version 3.0 available on 25th March due to cloud-coverage in the AERONET stations. For both events, the urban background air-quality surface station in Granada (Palacio de Congresos (PAL) http://juntadeandalucia.es/medioambiente) registered 10-minute PM_{10} concentrations, being up to 2500 μgm^{-3} on the 15th of March and up to 800 μgm^{-3} on the 25th of March, values that are way above the usual PM_{10} values (~100 μgm^{-3}) registered at Granada during usual dust outbreaks (Párraga et al., 2021). In this day, lidar measurements in AGORA in the framework of the European Aerosol Research Lidar Network (EARLINET; https://www.earlinet.org/) were saturated in the first 1-2 km and avoided any kind of retrieval of aerosol optical properties. Nevertheless, these measurements served to illustrate that most of the transport occurred in the first two kilometers above the ground.

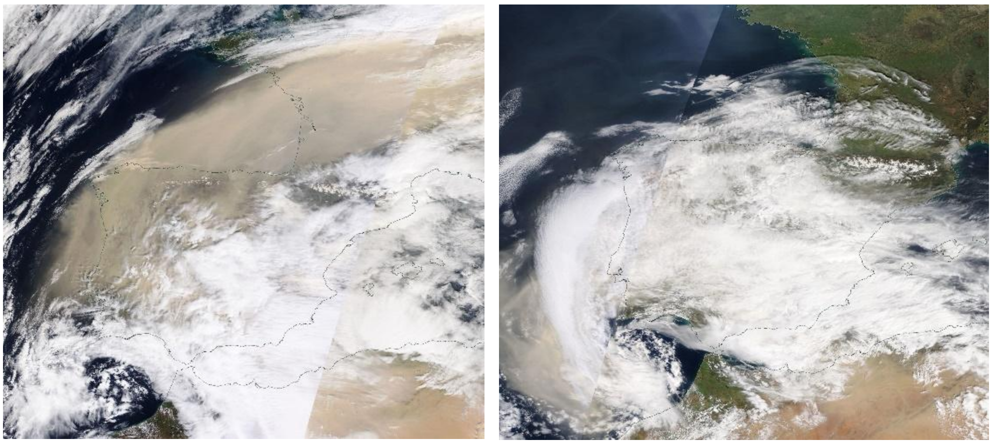

Figure 4. (a) Satellite image from 15th March 2022. (b) Satellite image from 25th March 2022. Images from https://wvs.earthdata.nasa.gov, obtained with MODIS (Moderate Resolution Imaging Spectroradiometer).

4 Results of aerosol phase matrix from different dust scenarios

4.1 Extreme events

For the two extreme events registered on 15th and 25th March 2022, Fig. 5 shows hourly averages of different aerosol properties obtained by the in-situ instruments at UGR station. In particular, we show eBC concentrations measured by the AE33, $\sigma_{sca}(\lambda)$ measured by the PI-Neph, and SAE, AAE (both calculated between 405 and 660 nm), $g(\lambda)$, $Bs(\lambda)$, $SSA(\lambda)$ and $LR(\lambda)$ derived from measurements of both instruments. PM_{10} concentrations are also shown, which were obtained from the PAL air-quality station (~ 600 m distance from UGR station). Panel (a) in Fig. 5 shows the results for the event on 15th - 16th March while Panel (b) are for the event on 24th - 25th March. Note that Panel (a) in Figure 5 does not cover the beginning of the Saharan dust event due to lack of data related to supersaturation of the PI-Neph's measurements.

For the event on 15th - 16th March, Fig. 5a.1 reveals extremely high PM_{10} with an average of 794 μgm^{-3} being over the regulatory daily limit value of 50 μgm^{-3} established by the Ambient Air Quality Directive (2008/50/CE European Directive). Maximum values of hourly PM_{10} concentrations are registered at around 16 UTC, with values up to 1800 μgm^{-3} approximately. The scattering coefficient time series shows the same behavior as the PM_{10}, with maximum values of σ_{sca} at the same time as the peak of the PM_{10} concentration. The mean value (±std) of SAE is 0.01 ± 0.15, which increases to 0.20 when PM_{10} concentrations reach their maximum. Such values of SAE suggest clear predominance of large particles. For the g parameter (Fig. 5a.4) approximately constant values are observed with mean values of 0.672 ± 0.010, 0.701 ± 0.006 and 0.729 ± 0.007 for 405, 515 and 660 nm, respectively, which are typical values for transported dust particles (Horvath et al., 2018). Also, Horvath et al. (2018) found an averaged Bs of 0.094 at 532 nm for Saharan dust, which agrees with the results shown in Fig. 5a.5 for the 515 nm wavelength (0.098 ± 0.003). The low values of the Bs observed at the three wavelengths are associated with small values of F_{11} at the backward scattering angles, which is common for non-spherical particles (Horvath et al., 2018). The lack of aethalometer data did not allow eBC, AAE, SSA and LR analyses for this day.

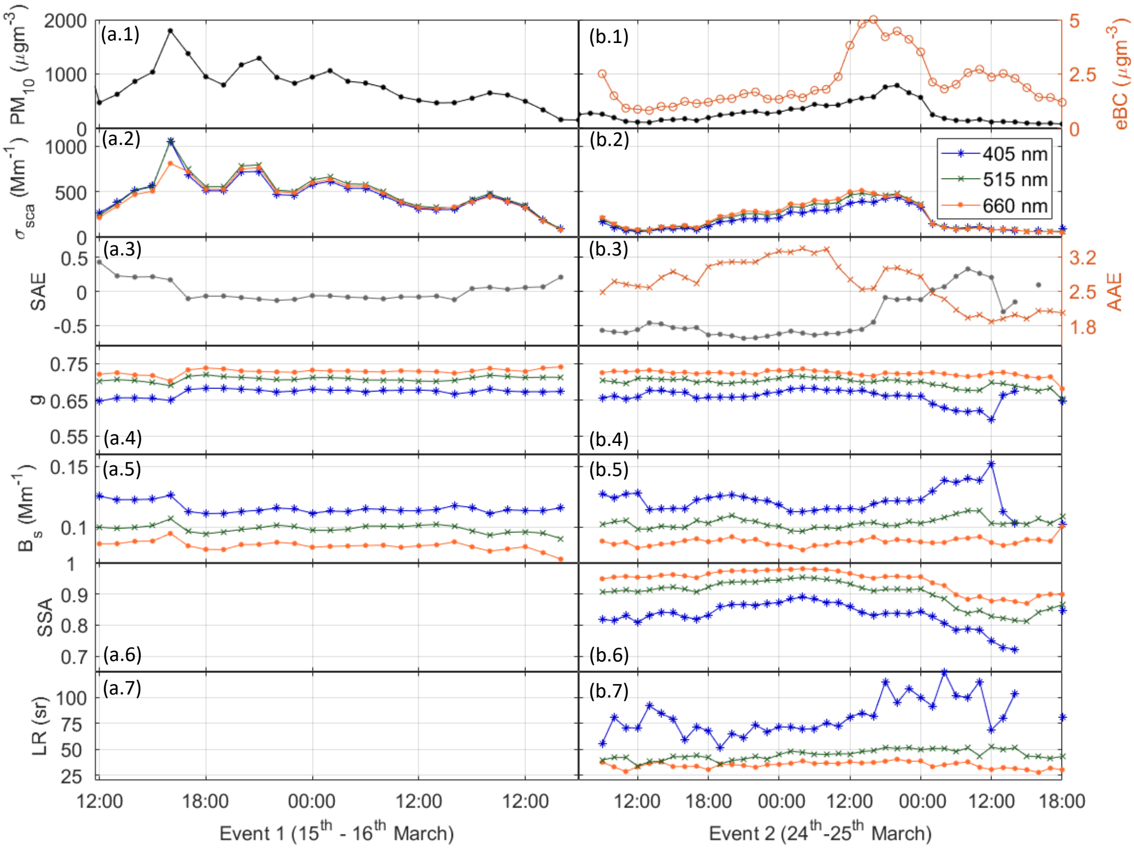

Figure 5. Time series of the PM$_{10}$ and eBC concentrations (a.1, b.1), σ_{sca} – scattering coefficient (a.2, b.2), SAE – scattering Angström exponent and AAE – absorption Angström exponent (a.3, b.3), g – asymmetry parameter (a.4, b.4), Bs – fraction of backscattered light (a.5, b.5), SSA – single scattering albedo (a.6, b.6) and LR – lidar ratio (a.7, b.7) for the extreme dust events of 15th March (a) and 24th March 2022 (b).

For the event on 24th - 25th March, the average PM$_{10}$ concentration is 283 µgm^{-3}. These PM$_{10}$ concentrations (Fig. 5b.1) increase until 10 UTC, when reach the maximum hourly value of 790 µgm^{-3}. These values are lower than those registered on 15th March, but again they are very high and above the daily limit of the European Directive. Scattering coefficients at the time of PM$_{10}$ concentration peak are 468, 476 and 441 Mm^{-1} for the 660, 515 and 405 nm wavelengths, respectively. After this peak, both PM$_{10}$ and σ_{sca} decrease, suggesting the end of the extreme dust outbreak. The SAE main feature is its approximately constant value of –0.5 until early in the morning on 25th March when it slightly starts to increase. This pattern suggests clear predominance of large particles during the dust outbreak, while the increase in the morning can be associated with additional influence of small particles, likely originated from road traffic during morning traffic rush hours (Lyamani et al., 2010a) On the other hand, the AAE shows a different behavior, with high values at the beginning of the time series representative of mineral dust and a later decrease to values around 1.7 coincident with the decrease in PM$_{10}$. These values of AAE are in the range of those reported by Valenzuela et al., (2015) for mixture of dust and black carbon particles, and also agrees with the patterns of eBC and PM$_{10}$ that suggest a larger contribution of eBC to the total PM$_{10}$ concentration at the end of the dust event than at the peak. On the other hand, g mean values are 0.659 ± 0.020, 0.698 ± 0.013 and 0.723 ± 0.009 for 405, 515 and 660 nm, respectively, being very similar to those observed on the other extreme event on 15th – 16th March. For the Bs (Fig.5.5) again is observed a similar behavior to the previous event (Fig. 5a.5), with values around 0.1 for the 515 nm wavelength and below 0.15 in the three channels. The channel at 405 nm seems to be the most sensitive in g and Bs to changes in dust concentration since the time when a sharp change happens (25th March at 14:00 UTC) coincides with the hour when PM$_{10}$ decreases and eBC increases indicating more contribution of eBC to the total ensemble of particles.

Aethalometer measurements during 24th-25th March allowed the study of further aerosol optical properties: the SSA (Fig. 5b.6) shows the highest values for all three wavelengths during the dust outbreaks. However, there is a strong spectral dependency, since the SSA at 405 nm clearly shows lower values (~0.85) compared to the other wavelengths, that present SSA above 0.9. As the PM$_{10}$ concentration decreases (and eBC concentration contribution to the mixture increases), the SSA shows smaller values with a stronger decrease in the 405 nm wavelength. Lastly, Fig. 5b.7 shows the time series of the LR during the second dust event, on 25th March. The LRs at 515 nm and 660 nm are rather constant, with mean values of 45 ± 5 sr and 35 ± 3 sr, respectively. However, the LR at 405 nm shows higher values and variability, with 81 ± 18 sr. LR at 515 nm is very similar to those measured by lidar systems at 532 nm for transported Saharan dust layers (Groß et al., 2013). Thus, the hypothesis that after 14:00 the presence of pollution particles becomes more relevant implies a decrease in SSA and illustrates variability in LRs, particularly in 405 nm.

Phase matrix elements were exhaustively monitored with the use of the PI-Neph during both extreme events. Given the high concentrations of large particles, the usual configuration of the measurements could lead to saturation of many angles in the forward scattering. Therefore, it was necessary to reduce the gain of the PI-Neph's camera, changing the dynamic range of the camera for obtaining non-saturated measurements at such high concentrations. But these changes were made to also guarantee enough signals in the backward region where the minimums are found. Nevertheless, sporadic pixels might present saturation/low SNR at some angles, but they were filtered out by the data quality criterion for the instrument (Section 2.2.1). For the specific phase function measurements where many data points are rejected, all angles are eliminated because phase matrix measurements were considered non-reliable. Moreover, $-F_{12}/F_{11}$ is computed by subtracting first parallel and perpendicular phase functions, that in many angles are very similar. Dividing this small number by F_{11} can enhance the differences, being particularly critical in the angular regions where the minimum values of scattering are found (typically between 90-150º for dust particles). All these effects, although they are always present, imply larger random noise in the measurements. Actually, noisier patterns in measured F_{11} and $-F_{12}/F_{11}$ affected by large particles when compared with measurements of anthropogenic origin have been already reported by the first versions of PI-Neph in the United States (Espinosa et al., 2018).

Figure 6 shows F_{11} and $-F_{12}/F_{11}$ phase matrix elements for the event on 15th - 16th March 2022 at four different representative stages. Data are 60-minutes averages, where the standard deviations represent the variability of the different parcels of air sampled throughout the hour of measurements. These standard deviations are around 20% of the average values for F_{11} and ranging between 0.1 and 0.2 for $-F_{12}/F_{11}$. Note that the large standard deviation can be explained by the specific issues for the measurements of dust particles commented above. Detailed hourly evolutions can be found in the Supplementary Material (Figs. S1-S2). Mean hourly averages of intensive and extensive aerosol parameters for the time periods shown in Fig. 6 are given in Table 1, particularly PM_{10}, σ_{sca}, SAE, AAE and g – note that SSA and LR were not available due to the lack of Aethalometer data for that day. Error bars in Table 1 are the standard deviations of the hourly mean values. Just before the impact of the extreme dust plume on 15th March 07:00 UTC (Figure 6a) values of PM_{10} (~61 μgm^{-3}) and SAE (~1.65) can be considered as background in the station and represent a mixture between fine and coarse mode particles. Later, on 15th March 12:00 UTC (Figure 6b) the drastic increase in PM_{10} (~473 μgm^{-3}) and decrease in SAE (~0.43) highlight a much larger contribution of coarse mode particles. Extreme values of PM_{10} of ~1375 μgm^{-3} on 15th March 17:00 UTC (Figure 6c) corresponds to the peak of the event. The lowest SAE (-0.11) was registered at that moment, and therefore a large contribution of coarse particles is expected. Finally, on 16th March 13:00 UTC (Figure 6d) the decrease in PM10 (~338 μgm^{-3}) plus the increase in SAE (~0.07) seems to indicate that the Saharan dust plume starts to withdraw.

Figure 6 shows a general pattern in F_{11} characterized by strong predominance of forward scattering up to two orders of magnitude greater than backward scattering. However, there are significant changes in both magnitudes and spectral dependence over time, that is, with the intensity of the dust outbreak passage. At the beginning of the dust event (Fig. 6a), the values of F_{11} in the forward scattering region are around 1000 $Mm^{-1}sr^{-1}$ for all three wavelengths, which is even one order of magnitude lower when compared with the cases at the other moments of the event (i.e. 50000 $Mm^{-1}sr^{-1}$ for the three channels during the peak). Also, at the beginning of the event (Fig. 6a) notable spectral separation in F_{11} is observed while such spectral separation is negligible during the rest of the event when coarse mode particles largely predominate. All F_{11} show the minimum in the region 120º-140º but the magnitude of that minimum varies between the different stages. Also, around that minimum is the region where some spectral difference is observed during the cases of strong predominance of coarse mode (Fig. 6c-d). A recovery from that minimum is also observed, being more pronounced in the cases close to the peak of the event.

Figure 6 shows that the differences in $-F_{12}/F_{11}$ patterns and wavelengths dependences with time are more remarkable than those observed for F_{11}. At the beginning $-F_{12}/F_{11}$ shows very different spectral patterns with remarkable spectral separation: for 515 and 660 nm, $-F_{12}/F_{11}$ follows bell-shaped patterns with values near to zero at the edges (0° and 180°) and a maximum around 90° of 0.4 and 0.5 for 515 and 660 nm, respectively. However, for 405 nm, the pattern is markedly different, with maximum values of 0.1 occurring at around 80°, followed by a sharp decrease, reaching negative values of -0.4 close to 150°. For the two following cases (Figs. 6b.2 and 6c.2), which are close to the peaks of maximum intensity in the Saharan dust outbreak, $-F_{12}/F_{11}$ shows a distinct pattern characterized by almost negligible differences with wavelength and a very small bell-shaped pattern with maxima around 0.1 at ~90°. Later, after the strong dust passage, Fig. 6d.2 shows for $-F_{12}/F_{11}$ a similar bell-shape pattern at 515 and 660 nm, but there is presence of some negative values at 405 nm.

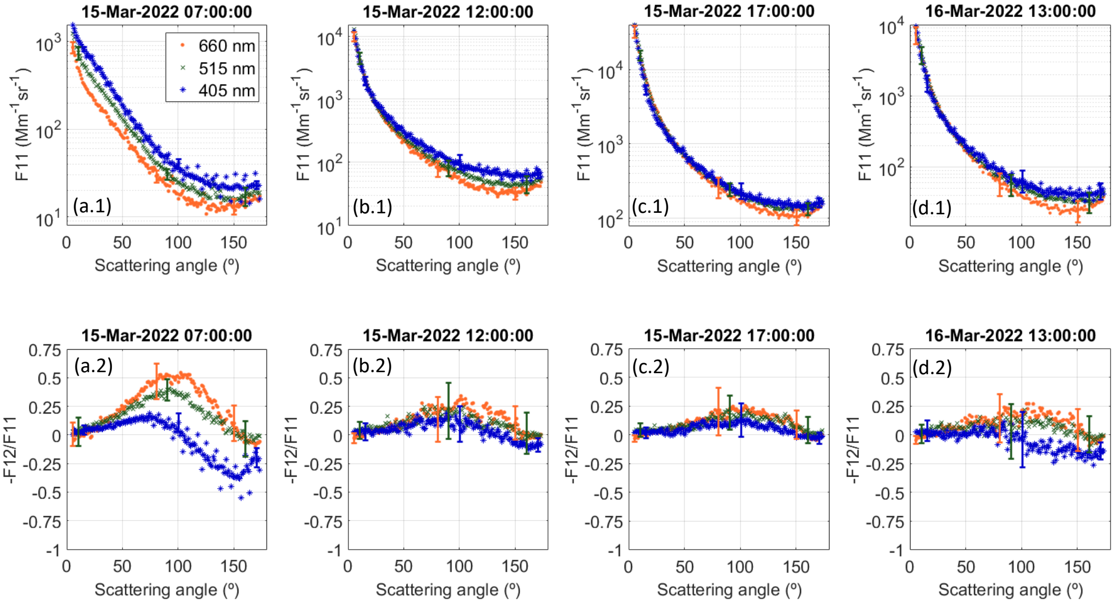

Figure 6. Hourly averages of phase function (F_{11}) and polarized phase function ($-F_{12}/F_{11}$) on 15th - 16th March 2022 for four different stages of the evolution of the extreme Saharan dust outbreak: (a) 15th March 07:00 UTC before the Saharan dust outbreak reached the station, (b) 15th March 12:00 UTC when the Saharan dust begins to reach the station, (c) 15th March 17:00 UTC associated with the peak of the extreme Saharan dust intrusion, and (d) 16th March 13:00 UTC when Saharan dust starts to withdrawn. Error bars correspond to the standard deviation of the hourly averages.

For the event on 24th - 25th March Fig. 7 shows F_{11} and $-F_{12}/F_{11}$ phase matrix elements for four different representative instants during the event. The data correspond again to 60-minute averages, with detailed hourly evolutions shown in the Supplementary Material (Figs. S3-S4), where the standard deviations represent the variability of the samples. These standard deviations are around 20% of the average values for F_{11} and around 0.2 for $-F_{12}/F_{11}$, showing larger variability during this dust event than in the previous one. Again, the specific issues related to the measurements of large particles can explain the deviations. Nevertheless, the larger deviations when compared with the previous events make us think that during this event there were more aerosol variability that is critical for the regions of the minimums in scattering. Mean hourly averages for these periods of intensive and extensive aerosol variables are again in Table 1, but now Aethalometer measurements permitted to add EBC, SSA and LR. Once again, this event exhibits lower values in particulate matter and appears to be less intense when compared to the event on 15th -16th March. However, it can still be considered an extreme event because the maximum PM_{10} concentrations (> 700 μgm^{-3}) registered are above the typical values (~100 μgm^{-3}) of Saharan dust transport to the UGR station (Parraga et al., 2021). Table 1 results serve to understand the temporal evolution of the extreme Saharan dust outbreak. On 24th March 13:00 UTC the lowest PM_{10} (~108 μgm^{-3}) are registered and can be associated with the background conditions before the intense outbreak. On 24th March 21:00 UTC the PM_{10} values (~297 μgm^{-3}) are almost three times those registered at noon and is associated with the entrance of the extreme event, while at on 25th March 09:00 UTC the largest PM_{10} values (~796 μgm^{-3}) are registered and that moment can be associated with the peak of the event. Finally, on 25th March 20:00 UTC the lowest values of PM_{10} (~116 μgm^{-3}) and associate that moment with the withdrawal of the extreme event. For the cases of very high PM_{10} (> 300 μgm^{-3}), although they present the largest eBC, the values of SAE and AAE suggest large predominance of coarse mode particles. But for the rest of the cases the mixture seems more complicated, and no conclusive claim can be made initially about the predominance of any kind of particles.

Figure 7 shows that F_{11} patterns are very similar to the previous extreme event on 15th - 16th March, with strong predominance of forward scattering (~25000 $Mm^{-1}sr^{-1}$), being two orders of magnitude above the backscattering (~100 $Mm^{-1}sr^{-1}$) at the peak of the event on 25th March 9:00 UTC. There are no significant spectral differences, as also happened for the other extreme event on 15th-16th March. These patterns in F_{11} agree with laboratory measurements of dust samples (i.e. Muñoz et al., 2007; Renard et al., 2014; Volten et al., 2001). Nevertheless, there are some features in F_{11} with the different situations: the slope in F_{11} in the forward scattering region becomes sharper when the PM_{10} concentrations are higher (Figs. 7b.1 and 7c.1). For the backward region F_{11} shows a flatter behavior for high PM_{10} concentrations (Figs. 7b.1 and 7.c.1), while for the cases with lower PM_{10} concentrations there is a sharp increase in scattering from 150° to 180°. During the previous extreme dust outbreak, we observed flat patterns for the backward scattering region during the peaks of the dust intrusions.

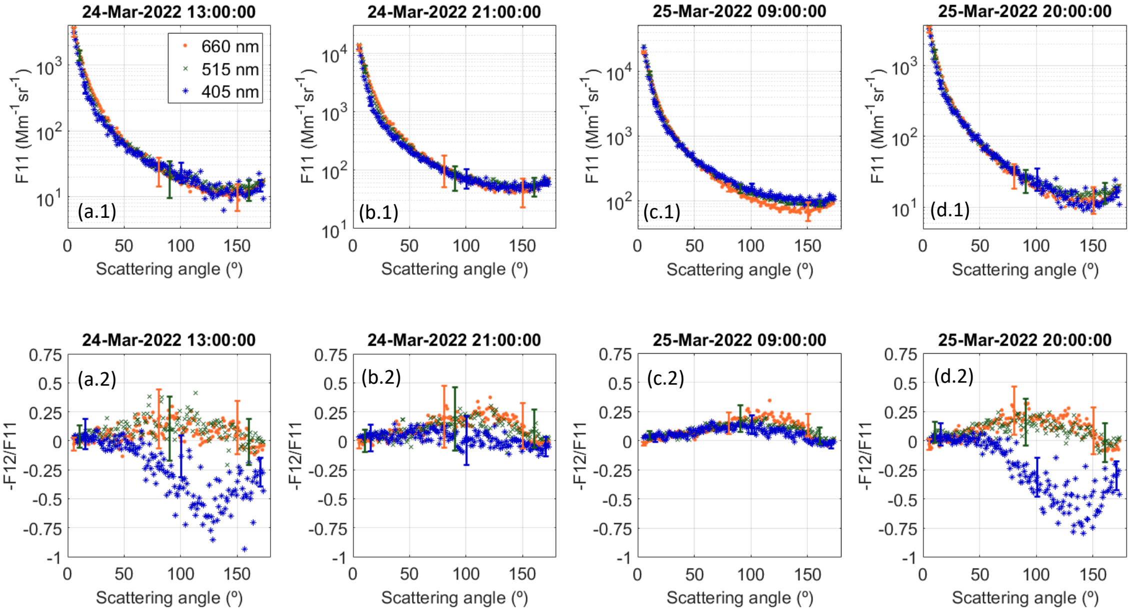

Figure 7. Hourly averages of phase function (F_{11}) and polarized phase function ($-F_{12}/F_{11}$) on 24th - 25th March 2022 for four different stages of the evolution of the extreme Saharan dust outbreak: (a) 24th March 13:00 UTC before the Saharan dust outbreak reached the station, (b) 24th March 21:00 UTC when the Saharan dust starts to reach the station, (c) 25th March 09:00 UTC associated with the peak of the extreme Saharan dust outbreak, and 25th March 20:00 UTC when dust begins to withdrawn. Error bars correspond to the standard deviation of the hourly averages.

Measurements of $-F_{12}/F_{11}$ in Figure 7 exhibit several behaviors throughout the event. During the peaks of the event on 24th-25th March (Fig. 7b-c), $-F_{12}/F_{11}$ patterns show minimal differences with wavelength and a very small bell-shaped pattern with maximums around 0.1 at 100°. However, there are differences when compared to the instants before the arrival of the dust outbreak (Fig. 7a) and when the dust is withdrawing (Fig. 7d). In these two cases $-F_{12}/F_{11}$ shows bell-shape patterns for 515 and 660 nm, with maximums of approximately 0.2 around 100° and values close to zero in the regions for scattering angles below 50° and above 150°. These patterns in $-F_{12}/F_{11}$ agree with the observed for the other instants of the event. However, the pattern for 405 nm is markedly different from the rest, and it is characterized by almost flat values close to zero of $-F_{12}/F_{11}$ in the range of approximately 0° - 50°, followed by a sharp decrease reaching negative values of -0.6 close to 130°. Then, there is a sharp increase in $-F_{12}/F_{11}$ reaching values close to zero at 180°. Therefore, $-F_{12}/F_{11}$ at 405 nm appears to be highly sensitive to the possible influence of other particles in the mixture. It is also noteworthy that the maximum in eBC coincides with the maximum of PM_{10}, but the contribution of eBC to the total aerosol burden is lower due to the high concentrations of dust. This can explain the dust-like pattern of -F_{12}/F_{11} at the peak of the event and the general agreement with laboratory measurements of dust samples (Muñoz et al., 2007b; Volten et al., 2001b).

Table 1. Hourly averaged properties of different stages of the extreme dust outbreaks in March 2022 reported in Figs. 6 and 7. The properties are reported at three wavelengths in the order of 660, 515 and 405 nm from top to bottom. Only the angular range of the PI-Neph (5°-175°) is used as the integration range of σ_{sca}. Error bars correspond to the standard deviations of the hourly means.

	PM$_{10}$ (μgm^{-3})	eBC (μgm^{-3})	σ_{sca} (Mm^{-1})	SAE	AAE	g	Bs (Mm^{-1})	SSA	LR (sr)
15th Mar 07:00	61 ± 5	-	55 ± 3	1.65 ± 0.13	-	0.573 ± 0.015	0.135 ± 0.013	-	-
			84 ± 4			0.604 ± 0.018	0.117 ± 0.011		
			123 ± 7			0.616 ± 0.008	0.116 ± 0.004		
15th Mar 12:00	473 ± 131	-	215 ± 36	0.43 ± 0.13	-	0.722 ± 0.001	0.086 ± 0.005	-	-
			241 ± 38			0.703 ± 0.001	0.100 ± 0.007		
			265 ± 39			0.641 ± 0.001	0.126 ± 0.005		
15th Mar 17:00	1376 ± 256	-	718 ± 128	-0.11 ± 0.12	-	0.734 ± 0.008	0.084 ± 0.005	-	-
			746 ± 112			0.715 ± 0.009	0.096 ± 0.005		
			682 ± 101			0.679 ± 0.009	0.113 ± 0.006		
16th Mar 13:00	338 ± 48	-	178 ± 47	0.07 ± 0.13	-	0.739 ± 0.008	0.079 ± 0.005	-	-
			191 ± 52			0.713 ± 0.008	0.095 ± 0.005		
			184 ± 50			0.673 ± 0.011	0.113 ± 0.006		
24th Mar 13:00	108 ± 14	0.81 ± 0.10	76 ± 13	-0.46 ± 0.22	2.58 ± 0.10	0.733 ± 0.024	0.084 ± 0.014	0.955 ± 0.004	36 ± 10
			70 ± 12			0.709 ± 0.031	0.098 ± 0.020	0.912 ± 0.006	38 ± 11
			65 ± 8			0.664 ± 0.035	0.117 ± 0.018	0.832 ± 0.006	92 ± 20
24th Mar 21:00	297 ± 21	1.59 ± 0.14	284 ± 27	-0.69 ± 0.18	3.09 ± 0.03	0.725 ± 0.025	0.088 ± 0.016	0.975 ± 0.001	34 ± 4
			257 ± 25			0.701 ± 0.025	0.105 ± 0.017	0.940 ± 0.001	40 ± 6
			205 ± 16			0.659 ± 0.021	0.124 ± 0.015	0.867 ± 0.003	61 ± 16
25th Mar 09:00	760 ± 44	4.21 ± 0.21	466 ± 15	-0.09 ± 0.06	2.96 ± 0.05	0.725 ± 0.007	0.087 ± 0.005	0.957 ± 0.002	39 ± 5
			461 ± 17			0.705 ± 0.009	0.101 ± 0.006	0.915 ± 0.003	52 ± 6
			427 ± 14			0.662 ± 0.007	0.122 ± 0.005	0.838 ± 0.005	115 ± 8
25th Mar 20:00	116 ± 6	2.3 ± 0.5	80 ± 7	-0.16 ± 0.18	2.03 ± 0.08	0.722 ± 0.019	0.086 ± 0.011	0.876 ± 0.015	32 ± 7
			78 ± 6			0.689 ± 0.020	0.104 ± 0.014	0.815 ± 0.020	52 ± 18
			74 ± 3			0.667 ± 0.021	0.113 ± 0.011	0.722 ± 0.021	104 ± 10

4.2 Moderate dust events during spring/summer 2022

The PI-Neph also continuously operated from April to September 2022 and other events of Saharan dust transport were registered at the UGR station. However, these outbreaks did not exhibit such an extreme dust transport when compared with the events in March 2022. Actually, hourly averaged PM$_{10}$ levels were below 130 µgm^{-3} and σ_{sca} below 130 Mm^{-1}, which are typical values observed at the UGR station during Saharan dust outbreaks (Lyamani et al., 2010). For this entire period of measurements (Apr 14th to Sep 9th) Fig. 8 shows hourly averages of PM$_{10}$ and eBC concentrations, $\sigma_{sca}(\lambda)$, SAE, AAE (both calculated in the 405-660 nm range), g(λ), Bs(λ), SSA(λ) and LR(λ). For the identification of cases with influence of mineral dust particles, data shown in Fig. 8 are filtered out and correspond only to values of SAE< 1, which are used as a proxy for the presence of dust particles in the atmosphere (i.e. Lyamani et al., 2010; Teri et al., 2024).

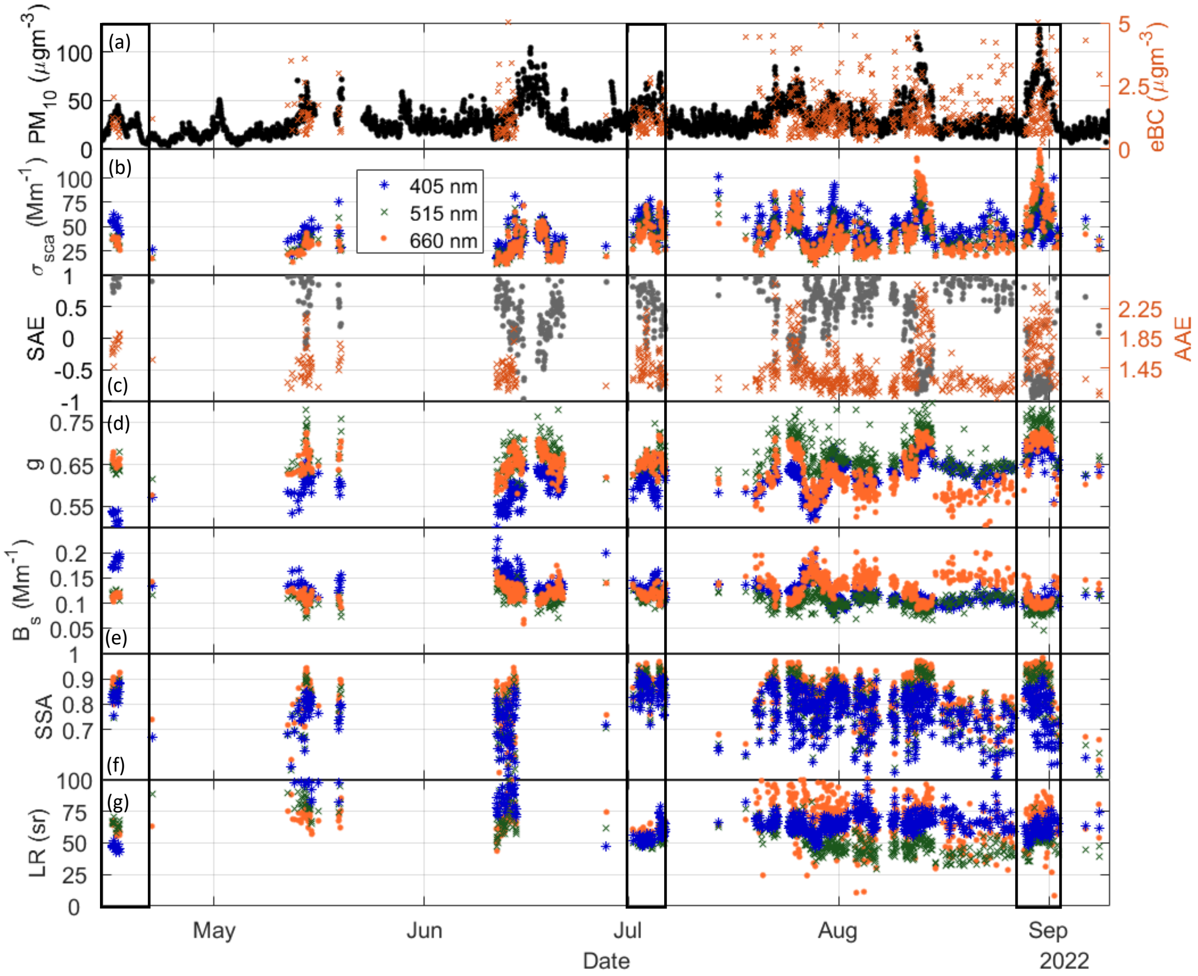

Figure 8. Time series for the moderate dust events of 2022 of the PM$_{10}$ and EBC concentrations (µgm^{-3}) (a), σ_{sca} – scattering coefficient (Mm^{-1}) (b), SAE – scattering Angström exponent and AAE – absorption Angström exponent (c), g – asymmetry parameter (d), Bs – fraction of backscattered light (Mm^{-1}) (e), SSA – single scattering albedo (f) and LR – lidar ratio (sr) (g). All optical properties are shown at 405, 515 and 660 nm. Black boxes represent three different events on 16th April, 5th July and 30th August 2022.

Figure 8 reveals that the period with the least frequency of dust events was April - June, although the few cases detected show high values of PM$_{10}$ concentrations and the scattering coefficients with SAE values closer to 1, suggesting a high degree of mixture between dust and pollution. Also, this period presents large spectral dependency in g and Bs, with g ranging between 0.5 and 0.7, and Bs ranging from 0.13-0.18, which are typical values more related to non-Saharan dust aerosols (Horvath et al., 2018). Moreover, SSA shows large variability ranging from 0.5 to around 0.9 for all three wavelengths, where the lower limit of the range suggests the presence of absorbing particles in the sample. This is also supported by the AAE with values close to 1, typical of BC.

During the summer season there is more frequency of Saharan dust intrusions, which is typical in the UGR station (Perez-Ramirez et al., 2016). Generally, there is more variability in all parameters, suggesting more complex mixtures of dust with other particles: the g parameter, which is wavelength dependent, shows very similar values to those obtained during spring, but with important variability ranging between 0.55 and 0.75. SAE and AAE show values between 0 and 1 and between 1 and 2, respectively, which are the typical values when there is influence of dust particles in our station (Valenzuela et al., 2015). The outliers in the summer season with negative SAE close to –0.5 and AAE of up to 2.5 might be associated with cases that have more presence of dust. In summer season the largest values of AAE (close to 2) are observed when compared with the spring season, which can be interpreted as fewer black carbon particles. SSA shows very similar values to those obtained during the spring season.

The LR is a critical variable for backscattered lidar systems and is an intensive aerosol variable that strongly depends on $F_{11}(180°)$ and absorption (Pérez-Ramírez et al., 2019). Because of that, LRs can be very sensitive to the different mixtures of particles in the atmosphere (Burton et al., 2012, 2013; Müller et al., 2007). Results of Fig. 8 serve to illustrate LR variability for dusty conditions but with the influence of other types of particles. Generally, Fig. 8 shows values between 40 sr and 100 sr for the three wavelengths. The lower limits are closer to the values for large predominance of dust (i.e. Müller et al., 2007) while the upper values are typical values registered for predominance of smoke/anthropogenic particles (Alados-Arboledas et al., 2011b; Burton et al., 2012, 2013; Floutsi et al., 2023; Müller et al., 2007). Thus, results of Fig. 8 indicate the large sensitivity of LR to changes in the mixture of particles. A seasonal analysis indicates that in spring – although there is less data – LRs are above 75 sr with little spectral dependence, suggesting more influence of fine particles in the mixture, which are ultimately responsible for LR values. During the summer seasons the lower values around 40-50 sr are more frequent, suggesting more predominance of coarse particles in the mixture.

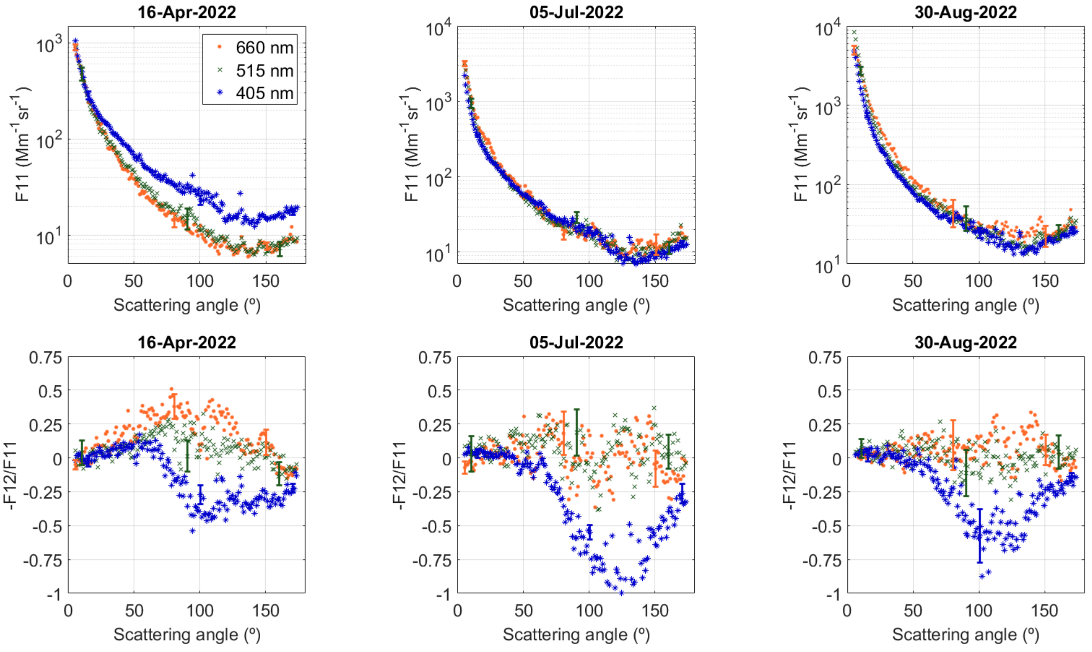

Figure 9. Phase function (F_{11}) and polarized phase function ($-F_{12}/F_{11}$) (for different moderate dust events: 15th April 202, 25th July 2022 and 30th August 2022. Error bars correspond to the standard deviation of the hourly averages.

To gain better understanding of the evolution of the phase matrix elements in different cases of dust mixtures with anthropogenic particles, Fig. 9 shows the phase matrix elements for three different dust events represented by the black boxes in Fig. 8. Particularly, Fig. 9 shows hourly averages of F_{11} and $-F_{12}/F_{11}$ representative of the peak in scattering during each event. Table 2 summarizes hourly mean values of PM_{10} and spectral σ_{sca}, g, Bs, LR and SSA, plus mean values of SAE and AAE for these selected cases. The standard deviations are larger (30% in in F_{11} and around 0.2 in $-F_{12}/F_{11}$) when compared with the extreme events, and despite the inherent issues in the measurement of phase matrix for large particles, it seems that the sample presents a more complex mixture with more variability during the 1-hour average.

The first event on 16th April is one of the most complex in terms of mixture of particles, with the lowest PM_{10} but with the largest SAE and AAE. The values of g suggest the lower contribution of dust particles when compared to the other cases (Horvath et al., 2018). The flat spectral pattern in SSA is the typical observed when there is contribution of fine mode particles of anthropogenic origin during a Saharan dust outbreak (Valenzuela et al., 2014). Nevertheless, the high AAE is not typical of black carbon and thus remarks the complexity of the mixture of aerosol particles in that day. For the case on 5th July the presence of mineral dust particles seems more relevant. The more pronounced spectral SSA when compared to 16th April also relates to the influence of dust in absorption (Dubovik et al., 2002), although the event on 5th July shows a lower AAE than for the previous case. Finally, the case on 30th August is the one with the largest PM_{10} concentrations but also with the largest eBC, which can make a very complex mixture. However, it should be noted that when affected by high concentrations of dust, the dust particles might interfere with the eBC measurements.

Table 2. Hourly averaged properties of different dust events in 2022. For properties reported at three wavelengths, the order is 660, 515 and 405 nm (top to bottom). The integration range of σ_{sca} is the angular range of the PI-Neph (5°-175°). Error bars are the standard deviations of the hourly means.

	PM_{10} (μgm^{-3})	eBC (μgm^{-3})	σ_{sca} (Mm^{-1})	SAE	AAE	g	Bs (Mm^{-1})	SSA	LR (sr)
16th Apr	36 ± 1	0.92 ± 0.14	31 ± 8	0.94 ± 0.88	1.71 ± 0.14	0.641 ± 0.024	0.119 ± 0.014	0.878 ± 0.017	59 ± 14
			31 ± 13			0.630 ± 0.036	0.126 ± 0.017	0.837 ± 0.028	61 ± 17
			48 ± 12			0.505 ± 0.005	0.193 ± 0.001	0.830 ± 0.008	43 ± 5
5th Jul	76 ± 1	1.07 ± 0.11	61 ± 5	-0.46 ± 0.07	1.37 ± 0.13	0.712 ± 0.035	0.097 ± 0.024	0.930 ± 0.004	61 ± 21
			53 ± 5			0.694 ± 0.060	0.109 ± 0.019	0.892 ± 0.016	58 ± 22
			49 ± 2			0.656 ± 0.016	0.114 ± 0.011	0.843 ± 0.007	66 ± 20
30th Aug	124 ± 2	2.42 ± 0.71	129 ± 5	-0.86 ± 0.11	1.73 ± 0.15	0.711 ± 0.019	0.096 ± 0.008	0.920 ± 0.021	67 ± 14
			115 ± 9			0.761 ± 0.021	0.080 ± 0.010	0.882 ± 0.028	58 ± 7
			85 ± 4			0.701 ± 0.009	0.104 ± 0.007	0.789 ± 0.032	63 ± 18

Figure 9 shows that all F_{11} cases exhibit the typical pattern for large and non-spherical particles characterized by large predominance of scattering in the forward region, although there is no remarkable flat behavior of the curve in the backward scattering which is characteristic of this type of particles from laboratory measurements (i.e Muñoz et al., 2007). However, there are differences between the events shown. In the case of the first dust event on 16th April (Fig. 9a), a strong spectral dependency is observed between 405 nm and the other wavelengths from 30° on, which is not observed for the other events. The largest contribution of urban pollution to the mixture can be one of the reasons for these spectral variations on 16th April. Another possible reason could be the less influence of absorbing particles as this case also presents the lower eBC and largest SSA when compared with the other two cases. The cases with almost negligible spectral differences could be explained by a more predominance of large particles. Thus, the discussion of these three selected cases illustrates that even though dust predominant cases present a classical scattering pattern characterized by strong forward scattering, the spectral dependences and the shape of the forward scattering depend ultimately on the mixture of particles. Note that all F_{11} are coherent with those obtained for the extreme dust outbreaks in March 2022, being the agreement more remarkable for the cases on 5th July and on 30th August.

Measurements of $-F_{12}/F_{11}$ in Fig. 9 present very similar patterns for the three cases. For 515 and 660 nm the $-F_{12}/F_{11}$ patterns are characterized by a bell-shape with large variability that might be associated with the complexity of the mixture of mineral dust and anthropogenic particles, as has been also observed for other dust particles measurements in the United States (Espinosa et al., 2018). However, the $-F_{12}/F_{11}$ pattern in

405 nm shows a very different behavior, having -F_{12}/F_{11} positive values until ~ 70° and negative -F_{12}/F_{11} values for the following angles. Minimum -F_{12}/F_{11} values are in the region around 120°. Therefore, -F_{12}/F_{11} measurements can be potentially used for investigating the mixture of particles in the sample. That pattern with negative values has been observed in the UGR station for cases with no influence of Saharan dust particles (Bazo et al., 2024), and also for biomass-burning at 473 nm (Espinosa et al., 2017). Nevertheless, there are differences between the three different cases that might be associated with the differences in the mixtures of aerosol particles.

5 Discussion

5.1 Comprehensive assessment of the different dust events

To gain more insight about aerosol mixtures during the extreme dust event on 24th – 25th March 2022 and the rest of dust cases registered in the period April – September 2022 we use the typing methodology defined in (Cazorla et al., 2013) and modified in (Schmeisser et al., 2017), based on optical properties. To that end, Fig. 10 shows SAE versus AAE, being both parameters computed in the range 450 -700 nm. For the SAE, we have used the σ_{sca} measured with the TSI integrating nephelometer since it directly provides measurements at the same wavelengths than those required in Schmeisser et al., (2017). The different types of aerosols are also illustrated in the Figure, where BC refers to black carbon and BrC to brown carbon in the definitions given by Schmeisser et al., (2017). Different colors are used to identify different stages in the temporal evolution for the extreme dust event on 24th – 25th March (Note that for the event on 15th – 16th March there were no aethalometer data and thus no measurements of AAE).

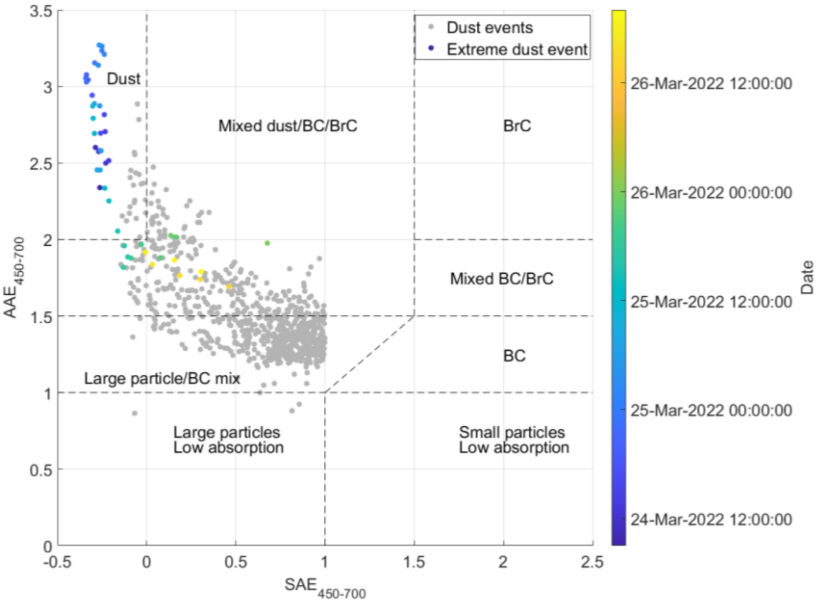

Figure 10. Absorption Angström exponent (AAE) versus scattering Angström exponent (SAE) for the extreme dust event on 24th - 25th March 2022 (colored markers) and for the moderate dust events registered in the UGR station during the period April-September 2022 (gray markers). Both intensive properties have been calculated in the range 450-700 nm. Colorbar indicates the temporal evolution of the extreme dust event on 24th - 25th March. Classification of different aerosol types following the method proposed by Schmeisser et al., (2017) is also shown.

Figure 10 shows that for the extreme dust outbreak on 24th- 25th March 2022 most of the data fall into the region of pure dust type, particularly those registered at beginning of the dust event when the PM_{10} concentrations were extremely high implying large predominance of coarse mineral dust particles. As the dust event evolves, particularly from 26th March 2022, the data points start to fall in the region mixed dust/BC/BrC. This coincides with the drop of PM_{10} concentration and the increase of eBC observed in Fig. 5. Therefore, there could be a more balanced contribution of both urban background pollution and mineral dust. If we compare these typing features with the scattering matrix elements on 24-25th March 2022 (Fig. 7), we observe that for the cases typed as pure dust the -F_{12}/F_{11} follows a bell-shape pattern for all wavelengths. However, for the cases classified as mixtures, there was a different pattern -F_{12}/F_{11} for the 405 nm channel. Thus, the typing classification explains the differences in the phase matrix for the temporal evolution of the extreme dust events during 15th-16th and 24th-25th March 2022 in the UGR station and show the potential of ground-based phase matrix measurements to distinguish between different types of aerosol mixtures.

For the rest of the analyzed period from April to September 2022 (classified as moderate events most in Fig. 8), most of the data falls into the region of large particle/BC mix and mixed dust/BC/BrC in Fig. 10. Since the UGR station is affected by local pollution (mainly road traffic) it is expected that the dust transported from the Saharan Desert gets mixed with the urban background pollution that is already suspended in the atmosphere. Another possibility is that dust already presents anthropogenic particles injected in the ensemble of particles during the transport process (Querol et al., 2019; Valenzuela et al., 2015). However, going further into the origin of these anthropogenic particles in the mixture is not possible with current data. In this study, the most important feature is that these possible mixtures can explain the differences in F_{11} and $-F_{12}/F_{11}$ between the extreme and moderate dust events, and also the different situations of dust mixtures in the station.

To further understand the behavior of the optical properties during different dust events, we have performed an average of all moderate dust events of the period April-September 2022 (filtered by $SAE < 0.5$ to guarantee more dust predominance) and compared it with the peaks of the extreme dust events, i.e. 15th March 2022 at 17:00 UTC and 25th March 2022 at 09:00 UTC. To this purpose, Fig. 11 shows F_{11} and $-F_{12}/F_{11}$ phase matrix elements for the different situations. For comparisons, we also include laboratory measurements of Saharan dust samples with the polar nephelometer in the Andalusian Institute of Astrophysics (Muñoz et al., 2010b), which are available in the Granada – Amsterdam Light Scattering Database (Muñoz et al., 2012). This database provides measurements of F_{11} and $-F_{12}/F_{11}$ at 488 and 632 nm - see Gómez Martín et al., (2021) for details. Results of F_{11} have been normalized with respect to $F_{11}(30°)$ to have the same scale for comparison.

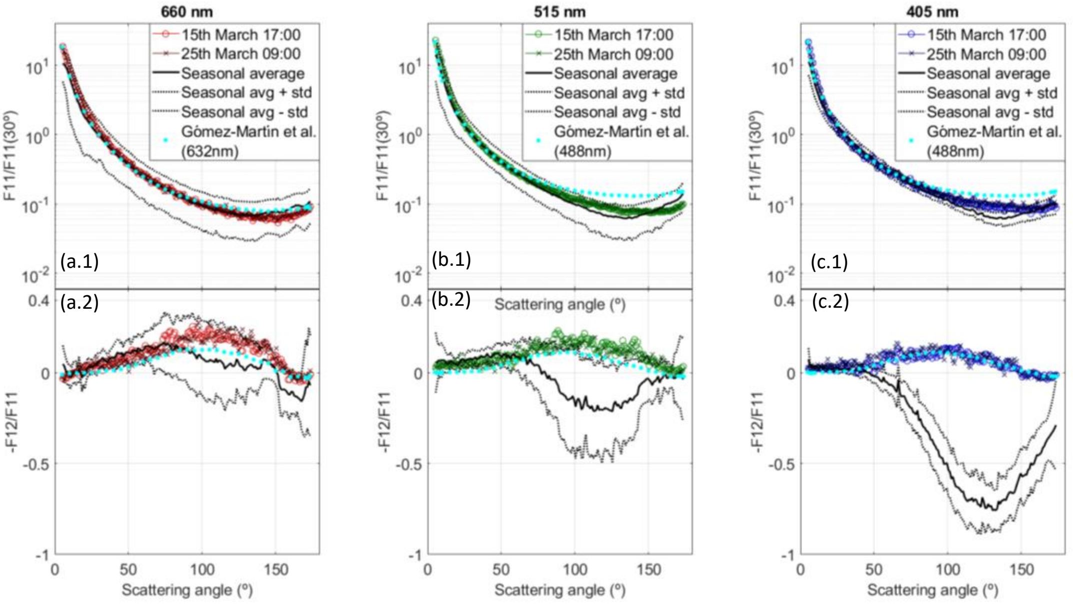

Figure 11. Phase function (F_{11}) (top) and polarized phase function ($-F_{12}/F_{11}$) (bottom) for different situations: Mean values for the cases obtained during moderate dust events (black lines), cases for extreme events on 15th March 2022 (red open circles) and on 25th March 2022 (red stars), and laboratory measurements at 632 nm and 488 nm (light blue dots) with samples collected in the Sahara and available in the Granada-Amsterdam Light Scattering database (Muñoz et al., 2012).

Figure 11 reveals that the F_{11} matrix element presents very similar features for the three wavelengths between mean averages for the period April-September 2022 and the extreme dust events, being the difference within the standard deviations. There are only slight differences in the forward region above 160° scattering angles, particularly for 515 nm channel, that might be associated by the complexity of the scattering at these angles for large and non-spherical particles ((Mischenko et al., 2002; Muñoz et al., 2007). Also, the small standard deviations of F_{11} are remarkable for the mean seasonal values, which suggest that F_{11} follows very similar patterns when there is predominance of large particles, independently of the mixture with other anthropogenic particles. Moreover, these patterns of F_{11} obtained from ambient aerosol basically coincide with those provided by the Light Scattering Database.

Figure 11 shows that seasonal values of $-F_{12}/F_{11}$ present in all cases larger standard deviations when compared to F_{11}. Particularly, for 660 and 515 nm large standard deviations are found in the region between 50º-150º while for 405 nm the standard deviations are considerably lower. Apart of the inherent limitations in the measurements in this scattering range, the results suggests that these $-F_{12}/F_{11}$ values at 660 and 515 nm are very sensitive to changing conditions in the aerosol that is sampled. Moreover, the other region that presents remarkable standard deviations for all wavelengths is the region of scattering angles above 170º. Those regions with large standard deviations are very sensitive to any change in particle type and size, which was demonstrated both from theoretical computations (Mischenko et al., 2002) and in laboratory measurements (Gomez-Martin et al., 2021). However, the lower standard deviations observed for the 405 nm wavelength indicate homogeneity in the response to polarization, even in the presence of other anthropogenic particles in the sample.

The comparison of means $-F_{12}/F_{11}$ between the different situations reveals very important features. Specifically, for 660 nm $-F_{12}/F_{11}$ follows a very similar pattern between the extreme events and the Light Scattering database. The mean seasonal average also follows the same pattern, but with a lower maximum and displaced to lower scattering regions. However, the 405 nm channel presents the most different behavior between the seasonal averages and the phase matrix elements for the dust events with two different patterns: For the extreme dust events and the Light Scattering Database, there is a bell shape pattern with values close to zero and a maximum of 0.1 at 100°, being the differences between both sets of data negligible. A different pattern is observed for the seasonal average, characterized by values around zero up to 50°, decreasing later to a minimum of -0.7 at 120° and increasing again to values close to 0 in the backward scattering region. Finally, the 515 nm channel presents an intermedia situation, being the extreme dust cases and the Light Scattering Database at 488 nm patterns very similar, while for the average of usual dust cases the pattern is like the observed at 405 but with less pronounced negative values.

The overall analysis of F_{11} and $-F_{12}/F_{11}$ phase matrix elements reveal that F_{11} patterns and spectral dependence is strongly affected by the existence of large and non-spherical particles, being the existence of other anthropogenic particles in the mixture affecting mainly the backscattering region. However, the possible existence of anthropogenic particles in the ensemble of particles characterized by predominance of large and non-spherical particles can affect importantly the values of $-F_{12}/F_{11}$ with strong wavelength-dependence. These changes are critical in the 405 nm channel being $-F_{12}/F_{11}$ negative values like that observed for pollution (i.e. Bazo et al., 2024) and biomass-burning at 473 nm (i.e. Espinosa et al., 2017). The 515 and 660 nm channels show $-F_{12}/F_{11}$ patterns more typical of pure dust measurements at laboratory (Muñoz et al., 2007; Renard et al., 2010). Therefore, polarization measurements have great potential for distinguishing different aerosol types in the mixture, which can be either internal or external mixtures of dust with other types of particles. Some model simulations even suggest that non-absorptive coating in mineral dust has a drastic variation in the behavior of $-F_{12}/F_{11}$ (Zhang et al., 2022, 2023), such as coatings of non-absorptive aerosol due to the long-range transport (Dall'Osto et al., 2010). Future works will focus on detailed studies of chemical analyses in combination with polar nephelometry measurements to further exploit the potential of polarization measurements in aerosol studies.

5.2 Phase matrix simulations for different aerosol mixture scenarios

To fully understand how different degrees of mixture between anthropogenic particles and mineral dust can affect F_{11} and $-F_{12}/F_{11}$, forward simulations with the Generalized Retrieval of Aerosol and Surface Properties algorithm (GRASP - Dubovik et al., 2014, 2021) have been performed. These simulations need inputs of different size distributions and refractive indexes to generate F_{11} and $-F_{12}/F_{11}$. Particularly, we used bi-lognormal size distribution, one representative of fine mode particles with modal radius of 0.15 µm and 0.25 µm of standard deviation and the other representative of coarse mode particles with modal radius of 2.5 µm and 1 µm of standard deviation. Real refractive indexes were assumed non-spectrally dependent with values of 1.6 for fine mode and 1.55 for coarse mode. Imaginary refractive indexes were 0.0015 for fine mode and with no spectral dependency, while for coarse mode there were of 0.007, 0.005 and 0.005 for 405, 515 and 660 nm. The sphere fraction was also fixed for each mode, being 0.7 for fine mode and 0.05 for coarse mode. The modal radii selected are close to those observed for the particle size distribution of the deposited particles in the UGR station (not shown for clarity). Moreover, the size distribution and refractive indexes selected can be considered representative of a mixture of anthropogenic pollution and dust (Torres et al., 2017). Three different scenarios were generated giving different weights to each mode: The first is for volume concentrations of 0.3 µm^3/µm^3 for each mode and can be considered as representative of a mixed case where both modes have a similar weight. The second presents more predominance of coarse mode (volume concentration of 0.5 µm^3/µm^3 for the coarse mode) but with non-negligible contribution of anthropogenic particles (volume concentrations of 0.1 µm^3/µm^3 for the fine mode). The last scenario is representative of pure dust mode (volume concentrations of 0.5 µm^3/µm^3) with negligible fine mode contribution (volume concentrations of 0.01 µm^3/µm^3). Results of computed F_{11} and $-F_{12}/F_{11}$ are in Fig. 12.

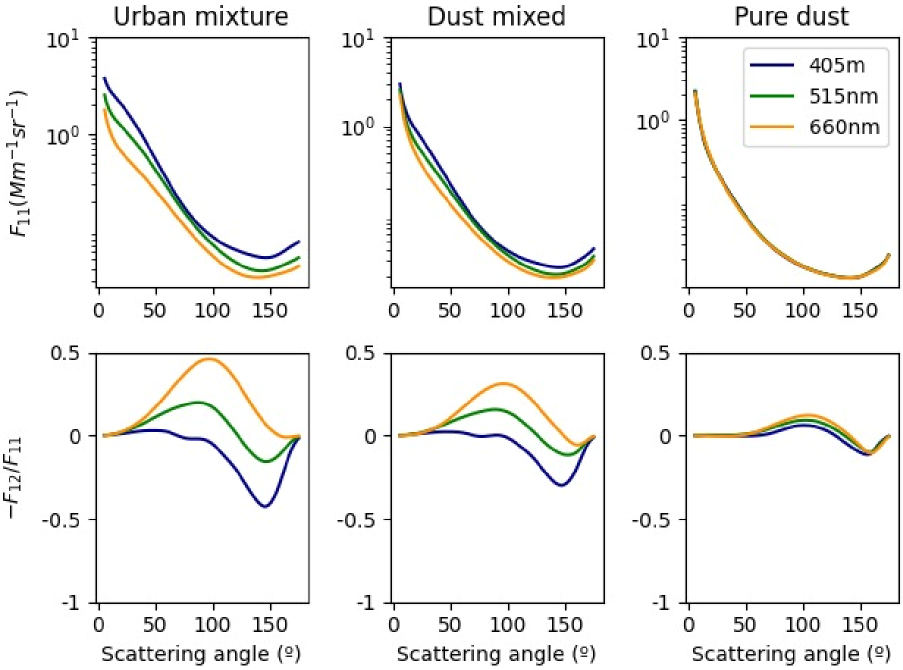

Figure 12. Simulations of phase function (F_{11}) and polarized phase function ($-F_{12}/F_{11}$) using GRASP forward for three different combinations of bi-lognormal size distributions. *Urban Mixture* with approximately the same weight of fine and coarse mode, *Dust mixed* with predominance of coarse mode but with a non-negligible influence of the fine mode, and *Pure Dust* with strong predominance of coarse mode and negligible fine mode. Note that refractive indexes and sphericity of each mode are different.

Figure 12 reveals important features in phase matrix elements depending on the mixture. For F_{11}, the patterns are generally characterized by larger forward scattering with minimums in the region of 120°-150°, independently on the type of aerosol mixture and on wavelength. The largest spectral dependencies are for the *Urban Mixture* case while for the other two cases such spectral dependencies become negligible. However, for $-F_{12}/F_{11}$ the largest variations in spectral dependencies and patterns are observed. In the *Urban Mixture* case the 660 nm channel shows a bell-shape pattern with maximum of ~ 0.4 in the region around 100°, while for 405 nm $-F_{12}/F_{11}$ shows approximately constants values close to zero until ~ 50° when it starts to decrease until the minimum of -0.5 in the region ~140°. Later it recovers reaching zero at 180°. On the other hand, for *Pure Dust* the $-F_{12}/F_{11}$ spectral dependencies are almost negligible, and it is characterized by a bell-shaped pattern with maximum around 0.2 in the region 110°-130°, with small negative values around 180º. Note that this feature is also present in the $-F_{12}/F_{11}$ in Figure 11 for the extreme dust cases, but it is not noticeable due to the scale. For the *Dust mixed* the pattern is in-between the previous ones.

Figure 12 results show how the presence of anthropogenic particles (fine mode) can alter the spectral dependencies in $-F_{12}/F_{11}$ when compared with only dust particles (coarse mode) in the sample, particularly in the blue channels. However, changes in the F_{11} patterns were not so evident. These results help to understand the different phase matrix elements discussed in this manuscript, and their temporal evolutions during the extreme dust events (Supplementary Material). However, studying the relationships between measured F_{11} and $-F_{12}/F_{11}$ with other aerosol optical and microphysical properties requires further analyses because F_{11} and $-F_{12}/F_{11}$ ultimately depend on the size distribution, refractive indexes, and particle shapes. The problem is even more complex if we differentiate optical properties between fine and coarse mode. Future optimization in GRASP will permit the retrieval of aerosol refractive indexes between fine and coarse mode separately using as inputs F_{11} and $-F_{12}/F_{11}$, and thus permitting further analyses of the different study cases discussed in this work. It is important to mention that the super-coarse mode can also affect the behavior of F_{11} and $-F_{12}/F_{11}$ and the presence of this mode is also observed for long-range transport (i.e. Renard et al., 2010). Future GRASP developments also need the consideration of this super-coarse mode. Another issue to study is the use of irregular-hexahedral for modeling the scattering of large and non-spherical particles that might reproduce better polarization signals (Saito and Yang, 2021, 2023; Saito et al., 2021).

6 Conclusions

This work has focused on the analyses of aerosol phase matrix elements and other optical properties during Saharan dust outbreaks that were registered in the UGR station (Southeastern Spain) in the year 2022. The main novelty of the analyses are the measurements by the multiwavelength Polarized Imaging Nephelometer (PI-Neph) developed by GRASP-Earth and capable of providing two aerosol scattering matrix elements (F_{11} and $-F_{12}/F_{11}$) for three different wavelengths (405, 515 and 660 nm). The uniqueness of PI-Neph is that it allows to measure phase matrix elements of ambient aerosol. The optimization of the instrument and the data quality check applied served to obtain (F_{11} and $-F_{12}/F_{11}$) with uncertainties below 10% and 20%, respectively. The multiwavelength F_{11} and $-F_{12}/F_{11}$ measurements for different Saharan dust outbreaks are some of the first carried out for ambient aerosol and serve to complement laboratory measurements of mineral dust particles and of synthetic samples minerals that compose dust particles. The novel measurements of F_{11} and $-F_{12}/F_{11}$ can also complement other optical and microphysical properties of Saharan dust already known from in-situ instrumentation and by active and passive remote sensing instruments, both from the ground and the space.

The analyses differentiate between two different scenarios: the first is two extreme Saharan dust outbreaks that happened on 15th – 16th (peaks in PM_{10} ~ 1800 μgm^{-3}) and on 25th – 26th March 2022 (peaks in PM_{10} ~ 690 μgm^{-3}) when the daily limit value of 50 μgm^{-3} delimited by the 2008/50/CE European Directive was exceeded. The detailed temporal evolution analysis of F_{11} for these extreme events did not show relevant changes with time, showing the classical pattern for predominance of big and non-spherical particles characterized by high predominance of forward scattering and almost negligible wavelength differences. For $-F_{12}/F_{11}$ at 515 and 660 nm there were no remarkable differences with time showing bell-shape pattern centered ~90° and with slightly positive values (maximums ~0.2). However, for 405 nm this bell-shape pattern was present only for the instants of extreme predominance of dust, while for the other instants $-F_{12}/F_{11}$ showed a very different pattern with values close to zero up to 50° - 60° followed by a decrease to values between -0.4 and -0.6 in the region around 120° and a final increase recovering to values close to zero in the backward region. On the other hand, the second analysis scenario was the period April – September 2022 when more moderate Saharan dust intrusions were registered (maximum PM_{10} around 100 μgm^{-3}. F_{11} mostly followed the classical pattern characterized by strong forward scattering, although some cases showed some spectral dependence on 405 nm depending on the influence of fine mode particles in the mixture. However, the analysis of $-F_{12}/F_{11}$ revealed big differences among wavelengths, being 405 nm like the pattern observed during the moments prior and after the peaks of the extreme dust events. The typing classification with additional in-situ measurements classified the peaks of the extreme dust events as pure dust while for the rest of measurements indicated a mixture of dust particles with local anthropogenic pollution, which can be the reason that explain the differences in $-F_{12}/F_{11}$. Thus, polarization at 405 nm seems to be very sensitive to the presence of additional anthropogenic particles in the sample dominated by mineral dust For 515 and 660 nm there are large variability depending on the mixture of particles. Nevertheless, more F_{11} and $-F_{12}/F_{11}$ measurements are needed at other experimental sites to have a more complete vision of mineral dust role on climate.

Laboratory measurements of mineral dust samples available in the Granada-Amsterdam Light Scattering Database provided F_{11} and $-F_{12}/F_{11}$ at 488 and 632 nm, allowing for a comparative assessment. To that end, averages of the period April – September 2022 plus the peaks of the extreme events during March 2022 were used. The results showed that for all normalized F_{11} the differences between temporal averages, peak events and laboratory measurements were minimal, being only notable in the backscattering region close to 180° where according to the T-Matrix theory more sensitive to aerosol particle parameters is found. For $-F_{12}/F_{11}$ laboratory measurements showed a bell-shape pattern with maximums around 0.2 in the region ~ 90° both at 488 and 632 nm, indicating very good agreement with the PI-Neph seasonal averages at 660 nm but important departures when comparing with 405 nm. However, during the peaks of the extreme dust events -F_{12}/F_{11} comparisons with laboratory measurements agree quite well. Considering that laboratory measurements consist of pure dust samples directly collected in the dessert, we can conclude that the -F_{12}/F_{11} at 405 nm measured in the laboratory is only reproduced when there are extreme concentrations of dust in the atmosphere, while the contribution of anthropogenic particles in the mixture the -F_{12}/F_{11} affects critically to -F_{12}/F_{11}. For the other channels, particularly 660 nm, -F_{12}/F_{11} seems to be less critically affected by the contribution of anthropogenic particles. We therefore believe that multiwavelength polarized polar nephelometry opens new possibilities in the studies of mineral dust role in the climate system.

Simulations performed by the GRASP code for different mixtures of fine mode (anthropogenic particles) and coarse mode (dust particles) revealed that F_{11} and -F_{12}/F_{11} are sensitive to the different contribution of each mode in the mixture, being especially critical for -F_{12}/F_{11} on the 405 nm channel. The negative values for -F_{12}/F_{11} in 405 nm were observed more clearly for the mixture of fine and coarse particles. Thus, these simulations have served to understand the experimental negative values in -F_{12}/F_{11} not observed in laboratory measurements for collected dust. Retrievals of bimodal size distribution with separate refractive indexes for each mode would have shown clarity to this problem. Hower, such retrieval with GRASP using F_{11} and -F_{12}/F_{11} as inputs needs to be optimized. Another additional optimization in GRASP will imply the possibility of implementing the retrieval of super-coarse mode particles. The possibility of implementing the irregular-hexahedral model would be also ideal to better understand polarization patterns. Nevertheless, the possibility of explaining the spectral differences in F_{11} and -F_{12}/F_{11} with wavelength has served to understand the temporal evolution of the extreme dust events and the difference and similitudes when comparing versus laboratory measurements and versus other more moderate events of Saharan dust transport. However, going further in understanding the interaction of dust with these anthropogenic particles requires further analyses that provide the chemical composition and size distribution of the ensemble of particles. This is planned in future studies that will allow a more complete comprehensive analysis.

Competing interests

The authors declare that they have no conflict of interest.

Author's contributions

EB analyzed the data and wrote the manuscript. DPR and FJO defined the structure of the paper, conceptualized the investigation and supervised the writing of the manuscript. ADZ analyzed the meteorological conditions during the extreme Saharan dust outbreaks. FR performed the GRASP simulations. FJO, AV and LAA are the principal investigators of the projects that funded the research and put the guidelines of the research. GT, AC, DP, FJGI assisted in the conceptualization. JVM and DF contributed to the development of the instrumentation. All authors contributed to the discussion of the results and provided comments on the paper.

Acknowledgments

This work was supported mainly by the Horizon Europe program under the Marie Sklodowska-Curie Staff Exchange Actions with the project GRASP-SYNERGY (grant agreement No 101131631). The work was also funded by the European Union's Horizon 2020 research and innovation program through projects ACTRIS.IMP (grant agreement No 871115) and ATMO_ACCESS (grant agreement No 101008004), and by the Spanish Ministry of Science and Innovation through projects ELPIS (PID2020-12001-5RB-I00), MULHACEN (PID2021-128008OB-I00), NUCLEUS (PID2021-128757OB-I00) funded by MICIU/AEI/10.13039/501100011033 and by ERDF A way of making Europe, and ACTRIS-España (RED2022-134824-E), and by University of Granada Plan Propio through Excellence Research Unit Earth Science and Singular Laboratory AGORA (LS2022-1) programs. E. Bazo received funding by MICIU/AEI/10.13039/501100011033 and the ESF + through FPI fellowship PRE2022-101272. F.J. García-Izquierdo acknowledges financial support from the grant PID2021-123370OB-I00 (CATS) funded by MCIN/AEI/10.13039/501100011033. We are very thankful to Air Quality Service of Junta de Andalucía for supplying the PM10 data.

References

Adebiyi, A. A., & Kok, J. F. Climate models miss most of the coarse dust in the atmosphere. *Sci. Adv.*, *6*(15). https://doi.org/10.1126/sciadv.aaz9507, 2020.

Adebiyi, A., Kok, J. F., Murray, B. J., Ryder, C. L., Stuut, J. B. W., Kahn, R. A., Knippertz, P., Formenti, P., Mahowald, N. M., Pérez García-Pando, C., Klose, M., Ansmann, A., Samset, B. H., Ito, A., Balkanski, Y., Di Biagio, C., Romanias, M. N., Huang, Y., & Meng, J. A review of coarse mineral dust in the Earth system. In *Aeolian Res.* (Vol. 60). Elsevier B.V. https://doi.org/10.1016/j.aeolia.2022.100849, 2023.

Ahern, A. T., Erdesz, F., Wagner, N. L., Brock, C. A., Lyu, M., Slovacek, K., Moore, R. H., Wiggins, E. B., & Murphy, D. M. Laser imaging nephelometer for aircraft deployment. *Atmos. Meas. Tech.*, *15*(5), 1093–1105. https://doi.org/10.5194/amt-15-1093-2022, 2022.

Alados-Arboledas, L., Müller, D., Guerrero-Rascado, J. L., Navas-Guzmán, F., Pérez-Ramírez, D., & Olmo, F. J. Optical and microphysical properties of fresh biomass burning aerosol retrieved by Raman lidar, and star-and sun-photometry. *Geophys. Res. Lett.*, *38*(1). https://doi.org/https://doi.org/10.1029/2010GL045999, 2011a.

Alados-Arboledas, L., Müller, D., Guerrero-Rascado, J. L., Navas-Guzmán, F., Pérez-Ramírez, D., & Olmo, F. J. Optical and microphysical properties of fresh biomass burning aerosol retrieved by Raman lidar, and star-and sun-photometry. *Geophys. Res. Lett.*, *38*(1). https://doi.org/10.1029/2010GL045999. 2011b.

Anderson, T. L., Covert, D. S., Marshall, S. F., Laucks, M. L., Charlson, R. J., Waggoner, A. P., Ogren, J. A., Caldow, R., Holm, R. L., Quant, F. R., Sem, G. J., Wiedensohler, A., Ahlquist, N. A., & Bates, T. S. Performance Characteristics of a High-Sensitivity, Three-Wavelength, Total Scatter/Backscatter Nephelometer. *J. Atmos. Ocean. Technol.*, *13*(5), 967–986. https://doi.org/10.1175/1520-0426(1996)013<0967:PCOAHS>2.0.CO;2, 1996.

Anderson, T. L., & Ogren, J. A. Determining Aerosol Radiative Properties Using the TSI 3563 Integrating Nephelometer. *Aerosol Sci. Tech.*, *29*(1), 57–69. https://doi.org/10.1080/02786829808965551, 1998.

Barkey, B., Liou, K. N., Gellerman, W., & Sokolsky, P. An Analog Light Scattering Experiment of Hexagonal Icelike Particles. Part I: Experimental Apparatus and Test Measurements. *J. Atmos. Sci.*, *56*(4), 605-612, https://doi.org/10.1175/1520-0469(1999)056<0605:AALSEO>2.0.CO;2, 1999.

Bazo, E., Granados-Muñoz, M. J., Román, R., Bravo-Aranda, J. A., Cazorla, A., Valenzuela, A., González, R., Olmo, F. J., & Alados-Arboledas, L. Evaluation of the vertically-resolved aerosol radiative effect on shortwave and longwave ranges using sun-sky photometer and ceilometer measurements. *Atmos. Res.*, *282*. https://doi.org/10.1016/j.atmosres.2022.106517, 2023.

Bazo, E., Martins, J. V., Perez-Ramirez, D., Valenzuela, A., Titos, G., Cazorla, A., Fuertes, D., Weiss, M., Turpie, A., Li, C., García-Izquierdo, F. J., Foyo-Moreno, I., Alados-Arboledas, L., & Olmo, F. J. Optimization of the Polarized Imaging Nephelometer (PI-Neph) for continuous monitoring of multiwavelength aerosol phase functions in support of space polarimetry missions. *Atmos. Environ.*, *316*, 120181. https://doi.org/10.1016/j.atmosenv.2023.120181, 2024.

Benedetti, A., Morcrette, J. -J., Boucher, O., Dethof, A., Engelen, R. J., Fisher, M., Flentje, H., Huneeus, N., Jones, L., Kaiser, J. W., Kinne, S., Mangold, A., Razinger, M., Simmons, A. J., & Suttie, M. Aerosol analysis and forecast in the European Centre for Medium-Range Weather Forecasts Integrated Forecast System: 2. Data assimilation. *J. Geophys. Res. Atmos.*, *114*(D13). https://doi.org/10.1029/2008JD011115, 2009.

Berkoff, T. A., Sorokin, M., Stone, T., Eck, T. F., Hoff, R., Welton, E., & Holben, B. Nocturnal aerosol optical depth measurements with a small-aperture automated photometer using the moon as a light source. *J. Atmos. Ocean. Technol.*, *28*(10), 1297–1306. https://doi.org/10.1175/JTECH-D-10-05036.1, 2011.

Bian, Y., Zhao, C., Xu, W., Zhao, G., Tao, J., & Kuang, Y. Development and validation of a CCD-laser aerosol detective system for measuring the ambient aerosol phase function. *Atmos. Meas. Tech.*, *10*(6), 2313–2322. https://doi.org/10.5194/amt-10-2313-2017, 2017.

Bodhaine, B. A., Ahlquist, N. C., & Schnell, R. C. (1991). Three-wavelength nephelometer suitable for aircraft measurement of background aerosol scattering coefficient. *Atmos. Environ.*, *25A*(10), 2267-2276. https://doi.org/10.1016/0960-1686(91)90102-D, 1991.

Burton, S. P., Ferrare, R. A., Hostetler, C. A., Hair, J. W., Rogers, R. R., Obland, M. D., Butler, C. F., Cook, A. L., Harper, D. B., & Froyd, K. D. Aerosol classification using airborne High Spectral Resolution Lidar measurements-methodology and examples. *Atmos. Meas. Tech.*, *5*(1), 73–98. https://doi.org/10.5194/amt-5-73-2012, 2012.

Burton, S. P., Ferrare, R. A., Vaughan, M. A., Omar, A. H., Rogers, R. R., Hostetler, C. A., & Hair, J. W. Aerosol classification from airborne HSRL and comparisons with the CALIPSO vertical feature mask. *Atmos. Meas. Tech.*, *6*(5), 1397–1412. https://doi.org/10.5194/amt-6-1397-2013, 2013.

Casquero-Vera, J. A., Pérez-Ramírez, D., Lyamani, H., Rejano, F., Casans, A., Titos, G., Olmo, F. J., Dada, L., Hakala, S., Hussein, T., Lehtipalo, K., Paasonen, P., Hyvärinen, A., Pérez, N., Querol, X., Rodríguez, S., Kalivitis, N., González, Y., Alghamdi, M. A., … Alados-Arboledas, L. Impact of desert dust on new particle formation events and the cloud condensation nuclei budget in dust-influenced areas. *Atmos. Chem. Phys.*, *23*(24), 15795–15814. https://doi.org/10.5194/acp-23-15795-2023, 2023.

Cazorla, A., Bahadur, R., Suski, K. J., Cahill, J. F., Chand, D., Schmid, B., Ramanathan, V., & Prather, K. A. Relating aerosol absorption due to soot, organic carbon, and dust to emission sources determined from in-situ chemical measurements. *Atmos. Chem. Phys.*, *13*(18), 9337–9350. https://doi.org/10.5194/acp-13-9337-2013, 2013.

Cazorla, A., Casquero-Vera, J. A., Román, R., Guerrero-Rascado, J. L., Toledano, C., Cachorro, V. E., Orza, J. A. G., Cancillo, M. L., Serrano, A., Titos, G., Pandolfi, M., Alastuey, A., Hanrieder, N., & Alados-Arboledas, L. Near-real-time processing of a ceilometer network assisted with sun-photometer data: monitoring a dust outbreak over the Iberian Peninsula. *Atmos. Chem. Phys.*, *17*(19), 11861–11876. https://doi.org/10.5194/acp-17-11861-2017, 2017.

Curtis, D. B., Aycibin, M., Young, M. A., Grassian, V. H., & Kleiber, P. D. Simultaneous measurement of light-scattering properties and particle size distribution for aerosols: Application to ammonium sulfate and quartz aerosol particles. *Atmos. Environ.*, *41*(22), 4748–4758. https://doi.org/10.1016/j.atmosenv.2007.03.020, 2007.

Curtis, D. B., Meland, B., Aycibin, M., Arnold, N. P., Grassian, V. H., Young, M. A., & Kleiber, P. D. A laboratory investigation of light scattering from representative components of mineral dust aerosol at a wavelength of 550 nm. *J. Geophys. Res. Atmos.*, *113*(8). https://doi.org/10.1029/2007JD009387, 2008.

Dall'Osto, M., Harrison, R. M., Highwood, E. J., O'Dowd, C., Ceburnis, D., Querol, X., & Achterberg, E. P. Variation of the mixing state of Saharan dust particles with atmospheric transport. *Atmos. Environ.*, *44*(26), 3135–3146. https://doi.org/10.1016/j.atmosenv.2010.05.030, 2010.

Daugeron, D., Renard, J.-B., Gaubicher, B., Couté, B., Hadamcik, E., Gensdarmes, F., Basso, G., & Fournier, C. Scattering properties of sands. 1. Comparison between different techniques of measurements. *Appl. Opt.*, *45*(32), 8331–8337. https://doi.org/10.1364/OA_License_v1#VOR, 2006.

Deuzé, J. L., Bréon, F. M., Deschamps, P. Y., Devaux, C., Herman, M., Podaire, A., & Roujean, J. L. Analysis of the POLDER (POLarization and directionality of earth's reflectances) airborne instrument observations over land surfaces. *Remote Sens. Environ.*, *45*(2), 137–154. https://doi.org/10.1016/0034-4257(93)90038-Y, 1993.

Di Biagio, C., Formenti, P., Balkanski, Y., Caponi, L., Cazaunau, M., Pangui, E., Journet, E., Nowak, S., Andreae, M. O., Kandler, K., Saeed, T., Piketh, S., Seibert, D., Williams, E., & Doussin, J. F.

Complex refractive indices and single-scattering albedo of global dust aerosols in the shortwave spectrum and relationship to size and iron content. *Atmos. Chem. Phys.*, *19*(24), 15503–15531. https://doi.org/10.5194/acp-19-15503-2019, 2019.

Di Biagio, C., Formenti, P., Balkanski, Y., Caponi, L., Cazaunau, M., Pangui, E., Journet, E., Nowak, S., Caquineau, S., Andreae, M. O., Kandler, K., Saeed, T., Piketh, S., Seibert, D., Williams, E., & Doussin, J.-F. Global scale variability of the mineral dust long-wave refractive index: a new dataset of in situ measurements for climate modeling and remote sensing. *Atmos. Chem. Phys.*, *17*(3), 1901–1929. https://doi.org/10.5194/acp-17-1901-2017, 2017.

Dolgos, G., & Martins, J. V. Polarized Imaging Nephelometer for in situ airborne measurements of aerosol light scattering. *Opt. Express*, *22*(18), 21972. https://doi.org/10.1364/oe.22.021972, 2014.

Drinovec, L., Močnik, G., Zotter, P., Prévôt, A. S. H., Ruckstuhl, C., Coz, E., Rupakheti, M., Sciare, J., Müller, T., Wiedensohler, A., & Hansen, A. D. A. The “dual-spot” Aethalometer: an improved measurement of aerosol black carbon with real-time loading compensation. *Atmos. Meas. Tech.*, *8*(5), 1965–1979. https://doi.org/10.5194/amt-8-1965-2015, 2015.

Dubovik, O., Fuertes, D., Litvinov, P., Lopatin, A., Lapyonok, T., Doubovik, I., Xu, F., Ducos, F., Chen, C., Torres, B., Derimian, Y., Li, L., Herreras-Giralda, M., Herrera, M., Karol, Y., Matar, C., Schuster, G. L., Espinosa, R., Puthukkudy, A., … Federspiel, C. A Comprehensive Description of Multi-Term LSM for Applying Multiple a Priori Constraints in Problems of Atmospheric Remote Sensing: GRASP Algorithm, Concept, and Applications. *Front. Remote Sens.*, *2*. https://doi.org/10.3389/frsen.2021.706851, 2021.

Dubovik, O., Holben, B., Eck, T. F., Smirnov, A., Kaufman, Y. J., King, M. D., Tanré, D., & Slutsker, I. Variability of Absorption and Optical Properties of Key Aerosol Types Observed in Worldwide Locations. *J. Atmos. Sci.*, *59*(3), 590–608. https://doi.org/10.1175/1520-0469(2002)059<0590:VOAAOP>2.0.CO;2, 2002.

Dubovik, O., & King, M. D. A flexible inversion algorithm for retrieval of aerosol optical properties from Sun and sky radiance measurements. *J. Geophys. Res. Atmos.*, *105*(D16), 20673–20696. https://doi.org/https://doi.org/10.1029/2000JD900282, 2000.

Dubovik, O., Lapyonok, T., Litvinov, P., Herman, M., Fuertes, D., Ducos, F., Lopatin, A., Chaikovsky, A., Torres, B., Derimian, Y., Huang, X., Aspetsberger, M., & Federspiel, C. GRASP: a versatile algorithm for characterizing the atmosphere. *SPIE Newsroom*. https://doi.org/10.1117/2.1201408.005558, 2014.

Dubovik, O., Li, Z., Mishchenko, M. I., Tanré, D., Karol, Y., Bojkov, B., Cairns, B., Diner, D. J., Espinosa, W. R., Goloub, P., Gu, X., Hasekamp, O., Hong, J., Hou, W., Knobelspiesse, K. D., Landgraf, J., Li, L., Litvinov, P., Liu, Y., … Yin, D. Polarimetric remote sensing of atmospheric aerosols: Instruments, methodologies, results, and perspectives. *J. Quant. Spectrosc. Radiat. Transf.*, *224*, 474–511. https://doi.org/10.1016/j.jqsrt.2018.11.024, 2019.

Dubovik, O., Sinyuk, A., Lapyonok, T., Holben, B. N., Mishchenko, M., Yang, P., Eck, T. F., Volten, H., Muñoz, O., Veihelmann, B., van der Zande, W. J., Leon, J.-F., Sorokin, M., & Slutsker, I. Application of spheroid models to account for aerosol particle nonsphericity in remote sensing of desert dust. *J. Geophys. Res. Atmos.*, *111*(D11). https://doi.org/https://doi.org/10.1029/2005JD006619, 2006.

Escudero, M., Castillo, S., Querol, X., Avila, A., Alarcón, M., Viana, M. M., Alastuey, A., Cuevas, E., & Rodríguez, S. Wet and dry African dust episodes over eastern Spain. *J. Geophys. Res. Atmos.*, *110*(D18). https://doi.org/10.1029/2004JD004731, 2005.

Espinosa, W. R., Martins, J. V., Remer, L. A., Puthukkudy, A., Orozco, D., & Dolgos, G. In situ measurements of angular-dependent light scattering by aerosols over the contiguous United States. *Atmos. Chem. Phys.*, *18*(5), 3737–3754. https://doi.org/10.5194/acp-18-3737-2018, 2018.

Espinosa, W. R., Remer, L. A., Dubovik, O., Ziemba, L., Beyersdorf, A., Orozco, D., Schuster, G., Lapyonok, T., Fuertes, D., & Martins, J. V. Retrievals of aerosol optical and microphysical properties from Imaging Polar Nephelometer scattering measurements. *Atmos. Meas. Tech.*, *10*(3), 811–824. https://doi.org/10.5194/amt-10-811-2017, 2017.

Fan, J., Wang, Y., Rosenfeld, D., & Liu, X. Review of Aerosol–Cloud Interactions: Mechanisms, Significance, and Challenges. *J. Atmos. Sci.*, *73*(11), 4221–4252. https://doi.org/10.1175/JAS-D-16-0037.1, 2016.

Fernández, A. J., Sicard, M., Costa, M. J., Guerrero Rascado, J., Gomez, J., Molero, F., Barragán, R., Basart, S., Bortoli, D., Bedoya-Velásquez, A., & et al. Extreme, wintertime Saharan dust intrusion in the Iberian Peninsula: lidar monitoring and evaluation of dust forecast models during the February 2017 event. *Atmos. Res.*, *228*, 223–241. https://doi.org/10.1016/j.atmosres.2019.06.007, 2019.

Floutsi, A. A., Baars, H., Engelmann, R., Althausen, D., Ansmann, A., Bohlmann, S., Heese, B., Hofer, J., Kanitz, T., Haarig, M., Ohneiser, K., Radenz, M., Seifert, P., Skupin, A., Yin, Z., Abdullaev, S. F., Komppula, M., Filioglou, M., Giannakaki, E., … Wandinger, U. DeLiAn - a growing collection of depolarization ratio, lidar ratio and Ångström exponent for different aerosol types and mixtures from ground-based lidar observations. *Atmos. Meas. Tech.*, *16*(9), 2353–2379. https://doi.org/10.5194/amt-16-2353-2023, 2023.

Formenti, P., Caquineau, S., Desboeufs, K., Klaver, A., Chevaillier, S., Journet, E., & Rajot, J. L. Mapping the physico-chemical properties of mineral dust in western Africa: mineralogical composition. *Atmos. Chem. Phys.*, *14*(19), 10663–10686. https://doi.org/10.5194/acp-14-10663-2014, 2014.

Formenti, P., Elbert, W., Maenhaut, W., Haywood, J., & Andreae, M. O. Chemical composition of mineral dust aerosol during the Saharan Dust Experiment (SHADE) airborne campaign in the Cape Verde region, September 2000. *J. Geophys. Res. Atmos.*, *108*(18). https://doi.org/10.1029/2002jd002648, 2003.

Forster, P. ., Storelvmo, T. ., Armour, K. ., Collins, W. ., Dufresne, J.-L. ., Frame, D. ., Lunt, D. J. ., Mauritsen, T. ., Palmer, M. D. ., Watanabe, M. ., Wild, M. ., & Zhang, H. The Earth's Energy Budget, Climate Feedbacks, and Climate Sensitivity. . In V. Masson-Delmotte, P. Zhai, A. Pirani, S. L. Connors, C. Péan, S. Berger, N. Caud, Y. Chen, L. Goldfarb, M. I. Gomis, M. Huang, K. Leitzell, E. Lonnoy, J. B. R. Matthews, T. K. Maycock, T. Waterfield, O. Yelekçi, R. Yu, & B. Zhou (Eds.), *Climate Change 2021: The Physical Science Basis. Contribution of Working Group I to the Sixth Assessment Report of the Intergovernmental Panel on Climate Change* (pp. 953–1054). Cambridge University Press, 2021.

Fuertes, D., Dubovik, O., Remer, L. A., Martins, J. V., Kleidman, R. G., & Federspiel, C. Calibrated high information content measurements from a commercial constellation of multi-angle polarimeters: The GAPMAP mission. *4S Symposium Portugal 2022*, 2022.

Gayet, J. F., Auriol, F., Oshchepkov, S., Schröder, F., Duroure, C., Febvre, G., Foumol, J. F., Crépel, O., Personne, P., & Daugereon, D. In situ measurements of the scattering phase function of stratocumulus, contrails and cirrus. *Geophys. Res. Lett.*, *25*(7), 971–974. https://doi.org/10.1029/98GL00541, 1998.

Gómez Martín, J. C., Guirado, D., Frattin, E., Bermudez-Edo, M., Cariñanos Gonzalez, P., Olmo Reyes, F. J., Nousiainen, T., Gutiérrez, P. J., Moreno, F., & Muñoz, O. On the application of scattering matrix measurements to detection and identification of major types of airborne aerosol particles: Volcanic ash, desert dust and pollen. *J. Quant. Spectrosc. Radiat. Transf.*, *271*. https://doi.org/10.1016/j.jqsrt.2021.107761, 2021.

Gonçalves Ageitos, M., Obiso, V., Miller, R. L., Jorba, O., Klose, M., Dawson, M., Balkanski, Y., Perlwitz, J., Basart, S., Di Tomaso, E., Escribano, J., Macchia, F., Montané, G., Mahowald, N. M., Green, R. O., Thompson, D. R., & Pérez García-Pando, C. Modeling dust mineralogical composition: sensitivity to soil mineralogy atlases and their expected climate impacts. *Atmos. Chem. Phys.*, *23*(15), 8623–8657. https://doi.org/10.5194/acp-23-8623-2023, 2023.

González-Flórez, C., Klose, M., Alastuey, A., Dupont, S., Escribano, J., Etyemezian, V., Gonzalez-Romero, A., Huang, Y., Kandler, K., Nikolich, G., Panta, A., Querol, X., Reche, C., Yus-Díez, J., &

Pérez García-Pando, C. Insights into the size-resolved dust emission from field measurements in the Moroccan Sahara. *Atmos. Chem. Phys.*, *23*(12), 7177–7212. https://doi.org/10.5194/acp-23-7177-2023, 2023.

González-Romero, A., González-Flórez, C., Panta, A., Yus-Díez, J., Reche, C., Córdoba, P., Moreno, N., Alastuey, A., Kandler, K., Klose, M., Baldo, C., Clark, R. N., Shi, Z., Querol, X., & Pérez García-Pando, C. Variability in sediment particle size, mineralogy, and Fe mode of occurrence across dust-source inland drainage basins: the case of the lower Drâa Valley, Morocco. *Atmos. Chem. Phys.*, *23*(24), 15815–15834. https://doi.org/10.5194/acp-23-15815-2023, 2023.

Groß, S., Esselborn, M., Weinzierl, B., Wirth, M., Fix, A., & Petzold, A. Aerosol classification by airborne high spectral resolution lidar observations. *Atmos. Chem. Phys.*, *13*(5), 2487–2505. https://doi.org/10.5194/acp-13-2487-2013, 2013.

Guerrero-Rascado, J. L., Olmo, F. J., Avilés-Rodríguez, I., Navas-Guzmán, F., Pérez-Ramírez, D., Lyamani, H., & Alados Arboledas, L. Extreme Saharan dust event over the southern Iberian Peninsula in september 2007: active and passive remote sensing from surface and satellite. *Atmos. Chem. Phys.*, *9*(21), 8453–8469. https://doi.org/10.5194/acp-9-8453-2009, 2009.

Haywood, J., and O. Boucher. Estimates of the direct and indirect radiative forcing due to tropospheric aerosols: A review, *Rev. Geophys.*, 38(4), 513–543. https://doi.org/10.1029/1999RG000078, 2000.

Holben, B. N., Eck, T. F., Slutsker, I., Tanré, D., Buis, J. P., Setzer, A., Vermote, E., Reagan, J. A., Kaufman, Y. J., Nakajima, T., Lavenu, F., Jankowiak, I., & Smirnov, A. AERONET—A Federated Instrument Network and Data Archive for Aerosol Characterization. *Remote Sens. Environ.*, *66*(1), 1–16. https://doi.org/https://doi.org/10.1016/S0034-4257(98)00031-5, 1998.

Holland, A. C., & Gagne, G. The Scattering of Polarized Light by Polydisperse Systems of rregular Particles, *Appl. Opt.*, *9*(5), 1113-1121. https://doi.org/10.1364/AO.9.001113, 1970.

Horvath, H. Extrapolation of a truncated aerosol volume scattering function to the far forward and back region. *J. Aerosol Sci.*, *90*, 26–35. https://doi.org/10.1016/j.jaerosci.2015.08.001, 2015.

Horvath, H., Alados Arboledas, L., & José Olmo Reyes, F. Angular scattering of the Sahara dust aerosol. *Atmos. Chem. Phys.*, *18*(23), 17735–17744. https://doi.org/10.5194/acp-18-17735-2018, 2018.

Hovenier, J. W., Volten, H., Muñoz, O., Van Der Zande, W. J., & Waters, L. B. F. M. Laboratory studies of scattering matrices for randomly oriented particles: potentials, problems, and perspectives. *J. Quant. Spectrosc. Radiat. Transf.*, *79-80*, 741-755. https://doi.org/10.1016/S0022-4073(02)00319-9, 2003.

Huang, Y., Kok, J. F., Martin, R. L., Swet, N., Katra, I., Gill, T. E., Reynolds, R. L., & Freire, L. S. Fine dust emissions from active sands at coastal Oceano Dunes, California. *Atmos. Chem. Phys.*, *19*(5), 2947–2964. https://doi.org/10.5194/acp-19-2947-2019, 2019.

Huang, Y., Liu, C., Yao, B., Yin, Y., & Bi, L. Scattering matrices of mineral dust aerosols: A refinement of the refractive index impact. *Atmos. Chem. Phys.*, *20*(5), 2865–2876. https://doi.org/10.5194/acp-20-2865-2020, 2020.

Jaggard, D., Hill, C., Stuart, D., Glantz, M., & Taggart, B. Light scattering from particles of regular and irregular shape. *Atmos. Environ.*, *15*(12), 2511-2519. https://doi.org/10.1016/0004-6981(81)90066-4, 1981.

Järvinen, E., Kemppinen, O., Nousiainen, T., Kociok, T., Möhler, O., Leisner, T., & Schnaiter, M. Laboratory investigations of mineral dust near-backscattering depolarization ratios. *J. Quant. Spectrosc. Radiat. Transf.*, *178*, 192–208. https://doi.org/10.1016/j.jqsrt.2016.02.003, 2016.

Kahn, R., Banerjee, P., McDonald, D., & Diner, D. J. Sensitivity of multiangle imaging to aerosol optical depth and to pure-particle size distribution and composition over ocean. *J. Geophys. Res. Atmos.*, *103*(D24), 32195–32213. https://doi.org/10.1029/98JD01752, 1988.

Kalnay, E., Kanamitsu, M., Kistler, R., Collins, W., Deaven, D., Gandin, L., Iredell, M., Saha, S., White, G., Woollen, J., Zhu, Y., Leetmaa, A., Reynolds, R., Chelliah, M., Ebisuzaki, W., Higgins, W., Janowiak, J., Mo, K. C., Ropelewski, C., … Joseph, D. The NCEP/NCAR 40-Year Reanalysis Project. *Bull. Am. Meteorol. Soc.*, *77*(3), 437–471. https://doi.org/10.1175/1520-0477(1996)077<0437:TNYRP>2.0.CO;2, 1996.

Kanamitsu, M., Ebisuzaki, W., Woollen, J., Yang, S.-K., Hnilo, J. J., Fiorino, M., & Potter, G. L. NCEP–DOE AMIP-II Reanalysis (R-2). *Bull. Am. Meteorol. Soc.*, *83*(11), 1631–1644. https://doi.org/10.1175/BAMS-83-11-1631, 2002.

King, M. D., Byrne, D. M., Herman, B. M., & Reagan, J. A. Aerosol Size Distributions Obtained by Inversions of Spectral Optical Depth Measurements. *J. Atmos. Sci.*, *35*(11), 2153–2167. https://doi.org/10.1175/1520-0469(1978)035<2153:ASDOBI>2.0.CO;2, 1978.

Kok, J. F., Adebiyi, A. A., Albani, S., Balkanski, Y., Checa-Garcia, R., Chin, M., Colarco, P. R., Hamilton, D. S., Huang, Y., Ito, A., Klose, M., Leung, D. M., Li, L., Mahowald, N. M., Miller, R. L., Obiso, V., Pérez García-Pando, C., Rocha-Lima, A., Wan, J. S., & Whicker, C. A. Improved representation of the global dust cycle using observational constraints on dust properties and abundance. *Atmos. Chem. Phys.*, *21*(10), 8127–8167. https://doi.org/10.5194/acp-21-8127-2021, 2021.

Kok, J. F., Ridley, D. A., Zhou, Q., Miller, R. L., Zhao, C., Heald, C. L., Ward, D. S., Albani, S., & Haustein, K. Smaller desert dust cooling effect estimated from analysis of dust size and abundance. *Nat. Geosci.*, *10*(4), 274–278. https://doi.org/10.1038/ngeo2912, 2017.

Kok, J. F., Ward, D. S., Mahowald, N. M., & Evan, A. T. Global and regional importance of the direct dust-climate feedback. *Nat. Comm.*, *9*(1), 241. https://doi.org/10.1038/s41467-017-02620-y, 2018.

Kuik, F., Stammes, P., & Hovenier, J. W. Experimental determination of scattering matrices of water droplets and quartz particles. *App. Opt.*, *30*(33), 4872–4861, https://doi.org/10.1364/AO.30.004872, 1991.

Levy, R. C., Remer, L. A., Mattoo, S., Vermote, E. F., & Kaufman, Y. J. Second-generation operational algorithm: Retrieval of aerosol properties over land from inversion of Moderate Resolution Imaging Spectroradiometer spectral reflectance. *J. Geophys. Res. Atmos.*, *112*(D13). https://doi.org/10.1029/2006JD007811, 2007.

Lyamani, H., Olmo, F. J., & Alados-Arboledas, L. Light scattering and absorption properties of aerosol particles in the urban environment of Granada, Spain. *Atmos. Environ.*, *42*(11), 2630–2642. https://doi.org/10.1016/j.atmosenv.2007.10.070, 2008.

Lyamani, H., Olmo, F. J., & Alados-Arboledas, L. Physical and optical properties of aerosols over an urban location in Spain: seasonal and diurnal variability. *Atmos. Chem. Phys.*, *10*(1), 239–254. https://doi.org/10.5194/acp-10-239-2010, 2010.

Manfred, K. M., Washenfelder, R. A., Wagner, N. L., Adler, G., Erdesz, F., Womack, C. C., Lamb, K. D., Schwarz, J. P., Franchin, A., Selimovic, V., Yokelson, R. J., & Murphy, D. M. Investigating biomass burning aerosol morphology using a laser imaging nephelometer. *Atmos. Chem. Phys.*, *18*(3), 1879–1894. https://doi.org/10.5194/acp-18-1879-2018, 2018.

Meland, B., Kleiber, P. D., Grassian, V. H., & Young, M. A. Correlated IR spectroscopy and visible light scattering measurements of mineral dust aerosol. *J. Geophys. Res. Atmos.*, *115*(20). https://doi.org/10.1029/2010JD014389, 2010.

Miffre, A., Cholleton, D., Noël, C., & Rairoux, P. Investigating the dependence of mineral dust depolarization on complex refractive index and size with a laboratory polarimeter at 180.0 lidar backscattering angle. *Atmos. Meas. Tech.*, *16*(2), 403–417. https://doi.org/10.5194/amt-16-403-2023, 2023.

Mischenko, M. I., & Travis, L. D. Light scattering by polydispersions of randomly oriented spheroids with sizes comparable to wavelengths of observations. *App. Opt.*, *33*(30), 7206- 7225. https://doi.org/10.1364/AO.33.007206, 1994.

Mischenko, M. I., & Travis, L. D. Satellite retrieval of aerosol properties over the ocean using polarization as well as intensity of reflected sunlight. *J. Geophys. Res.*, *102*(D14), 16989–17013. https://doi.org/10.1029/96JD02425, 1997.

Mischenko, M. I., Travis, L. D., & Lacis, A. A. *Scattering, Absorption, and Emission of Light by Small Particles* (First). Cambridge University Press, 2002.

Mishchenko, M. I., Cairns, B., Kopp, G., Schueler, C. F., Fafaul, B. A., Hansen, J. E., Hooker, R. J., Itchkawich, T., Maring, H. B., & Travis, L. D. Accurate Monitoring of Terrestrial Aerosols and Total Solar Irradiance: Introducing the Glory Mission. *Bull. Am. Meteorol. Soc.*, *88*(5), 677–692. https://doi.org/10.1175/BAMS-88-5-677, 2007.

Moallemi, A., Modini, R. L., Brem, B. T., Bertozzi, B., Giaccari, P., & Gysel-Beer, M. Concept, absolute calibration, and validation of a new benchtop laser imaging polar nephelometer. *Atmos. Meas. Tech.*, *16*(15), 3653–3678. https://doi.org/10.5194/amt-16-3653-2023, 2023.

Moallemi, A., Modini, R. L., Lapyonok, T., Lopatin, A., Fuertes, D., Dubovik, O., Giaccari, P., & Gysel-Beer, M. Information content and aerosol property retrieval potential for different types of in situ polar nephelometer data. *Atmos. Meas. Tech.*, *15*(19), 5619–5642. https://doi.org/10.5194/amt-15-5619-2022, 2022.

Morcrette, J. -J., Boucher, O., Jones, L., Salmond, D., Bechtold, P., Beljaars, A., Benedetti, A., Bonet, A., Kaiser, J. W., Razinger, M., Schulz, M., Serrar, S., Simmons, A. J., Sofiev, M., Suttie, M., Tompkins, A. M., & Untch, A. Aerosol analysis and forecast in the European Centre for Medium-Range Weather Forecasts Integrated Forecast System: Forward modeling. *J. Geophys. Res. Atmos.*, *114*(D6). https://doi.org/10.1029/2008JD011235, 2009.

Müller, D., Ansmann, A., Mattis, I., Tesche, M., Wandinger, U., Althausen, D., & Pisani, G. Aerosol-type-dependent lidar ratios observed with Raman lidar. *J. Geophys. Res. Atmos.*, *112*(16). https://doi.org/10.1029/2006JD008292, 2007.

Muñoz, O., Moreno, F., Guirado, D., Dabrowska, D. D., Volten, H., & Hovenier, J. W. The Amsterdam–Granada Light Scattering Database. *J. Quant. Spectrosc. Radiat. Transf.*, *113*(7), 565–574. https://doi.org/10.1016/j.jqsrt.2012.01.014, 2012.

Muñoz, O., Moreno, F., Guirado, D., Ramos, J. L., López, A., Girela, F., Jerónimo, J. M., Costillo, L. P., & Bustamante, IExperimental determination of scattering matrices of dust particles at visible wavelengths: The IAA light scattering apparatus. *J. Quant. Spectrosc. Radiat. Transf.*, *111*(1), 187–196. https://doi.org/10.1016/j.jqsrt.2009.06.011, 2010a.

Muñoz, O., Volten, H., Hovenier, J. W., Nousiainen, T., Muinonen, K., Guirado, D., Moreno, F., & Waters, L. B. F. M. Scattering matrix of large Saharan dust particles: Experiments and computations. *J. Geophys. Res. Atmos.*, *112*(13). https://doi.org/10.1029/2006JD008074, 2007a.

Nakajima, T., Tonna, G., Rao, R., Boi, P., Kaufman, Y., & Holben, B. Use of sky brightness measurements from ground for remote sensing of particulate polydispersions. *App. Opt.*, *35*(15), 2672. https://doi.org/10.1364/AO.35.002672, 1996.

Olmo, F. J., Quirantes, A., Alcántara, A., Lyamani, H., & Alados-Arboledas, L. Preliminary results of a non-spherical aerosol method for the retrieval of the atmospheric aerosol optical properties. *J. Quant. Spectrosc. Radiat. Transf.*, *100*(1–3), 305–314. https://doi.org/10.1016/j.jqsrt.2005.11.047, 2006.

Olmo, F. J., Quirantes, A., Lara, V., Lyamani, H., & Alados-Arboledas, L. Aerosol optical properties assessed by an inversion method using the solar principal plane for non-spherical particles. *J. Quant. Spectrosc. Radiat. Transf.*, *109*(8), 1504–1516. https://doi.org/10.1016/j.jqsrt.2007.12.019, 2008.

Ooki, A., & Uematsu, M. Chemical interactions between mineral dust particles and acid gases during Asian dust events. *J. Geophys. Res. Atmos.*, *110*(D3). https://doi.org/10.1029/2004JD004737, 2005.

Ortiz-Amezcua, P., Guerrero-Rascado, J. L., Granados-Muñoz, M. J., Benavent-Oltra, J. A., Böckmann, C., Samaras, S., Stachlewska, I. S., Janicka, Ł., Baars, H., Bohlmann, S., & Alados-Arboledas, L.

Microphysical characterization of long-range transported biomass burning particles from North America at three EARLINET stations. *Atmos. Chem. Phys.*, *17*(9), 5931–5946. https://doi.org/10.5194/acp-17-5931-2017, 2017.

Párraga, J., Martín-García, J. M., Delgado, G., Molinero-García, A., Cervera-Mata, A., Guerra, I., Fernández-González, M. V., Martín-Rodríguez, F. J., Lyamani, H., Casquero-Vera, J. A., Valenzuela, A., Olmo, F. J., & Delgado, R. Intrusions of dust and iberulites in Granada basin (Southern Iberian Peninsula). Genesis and formation of atmospheric iberulites. *Atmos. Res.*, *248*, 105260. https://doi.org/10.1016/j.atmosres.2020.105260, 2021.

Patrón, D., Lyamani, H., Titos, G., Casquero-Vera, J. A., Cardell, C., Močnik, G., Alados-Arboledas, L., & Olmo, F. J. Monumental heritage exposure to urban black carbon pollution. *Atmos. Environ.*, *170*, 22–32. https://doi.org/10.1016/J.ATMOSENV.2017.09.030, 2017.

Pérez-Ramírez, D., Lyamani, H., Olmo, F. J., & Alados-Arboledas, L. Improvements in star photometry for aerosol characterizations. *Journal of Aerosol Science*, *42*(10), 737–745. https://doi.org/10.1016/j.jaerosci.2011.06.010, 2011.

Pérez-Ramírez, D., Lyamani, H., Smirnov, A., O´Neill, N. T., Veselovskii, I., Whiteman, D. N., Olmo, F. J., & Alados-Arboledas, L. Statistical study of day and night hourly patterns of columnar aerosol properties using sun and star photometry, *SPIE Remote Sensing*. https://doi.org/10.1117/12.2242372, 2016.

Pérez-Ramírez, D., Ruiz, B., Aceituno, J., Olmo, F. J., & Alados-Arboledas, L. Application of Sun/star photometry to derive the aerosol optical depth. *Int. J. Remote Sens.*, *29*(17–18), 5113–5132. https://doi.org/10.1080/01431160802036425, 2008.

Pérez-Ramírez, D., Whiteman, D. N., Veselovskii, I., Colarco, P., Korenski, M., & da Silva, A. Retrievals of aerosol single scattering albedo by multiwavelength lidar measurements: Evaluations with NASA Langley HSRL-2 during discover-AQ field campaigns. *Remote Sens. Environ.*, *222*, 144–164. https://doi.org/10.1016/j.rse.2018.12.022, 2019.

Perry, R. J., Hunt, A. J., & Huffman, D. R. Experimental determinations of Mueller scattering matrices for nonspherical particles. *Applied Optics*, *17*(17), 2700–2710. https://doi.org/10.1364/AO.17.002700, 1978.

Petzold, A., & Schönlinner, M. Multi-angle absorption photometry—a new method for the measurement of aerosol light absorption and atmospheric black carbon. *J. Aerosol Sci.*, *35*(4), 421–441. https://doi.org/10.1016/J.JAEROSCI.2003.09.005, 2004.

Pope, S. K., Tomasko, M. G., Williams, M. S., Perry, M. L., Doose, L. R., & Smith, P. H. Clouds of Ammonia Ice: Laboratory Measurements of the Single-Scattering Properties. In *ICARUS 100*(1), 203-220. https://doi.org/10.1016/0019-1035(92)90030-B, 1992.

Puthukkudy, A., Martins, J. V., Remer, L. A., Xu, X., Dubovik, O., Litvinov, P., McBride, B., Burton, S., & Barbosa, H. M. J. Retrieval of aerosol properties from Airborne Hyper-Angular Rainbow Polarimeter (AirHARP) observations during ACEPOL 2017. *Atmos. Meas. Tech.*, *13*(10), 5207–5236. https://doi.org/10.5194/amt-13-5207-2020, 2020.

Querol, X., Pérez, N., Reche, C., Ealo, M., Ripoll, A., Tur, J., Pandolfi, M., Pey, J., Salvador, P., Moreno, T., & Alastuey, A. African dust and air quality over Spain: Is it only dust that matters? *Sci. Tot. Environ.*, *686*, 737–752. https://doi.org/10.1016/j.scitotenv.2019.05.349, 2019.

Remer, L. A., Davis, A. B., Mattoo, S., Levy, R. C., Kalashnikova, O. V., Coddington, O., Chowdhary, J., Knobelspiesse, K., Xu, X., Ahmad, Z., Boss, E., Cairns, B., Dierssen, H. M., Diner, D. J., Franz, B., Frouin, R., Gao, B.-C., Ibrahim, A., Martins, J. V., … Zhai, P.-W. Retrieving Aerosol Characteristics From the PACE Mission, Part 1: Ocean Color Instrument. *Front. Earth Sci.*, *7*. https://doi.org/10.3389/feart.2019.00152, 2019.

Renard, J. B., Dulac, F., Durand, P., Bourgeois, Q., Denjean, C., Vignelles, D., Couté, B., Jeannot, M., Verdier, N., & Mallet, M. In situ measurements of desert dust particles above the western

Mediterranean Sea with the balloon-borne Light Optical Aerosol Counter/sizer (LOAC) during the ChArMEx campaign of summer 2013. *Atmos. Chem. Phys.*, *18*(5), 3677–3699. https://doi.org/10.5194/acp-18-3677-2018, 2018.

Renard, J. B., Hadamcik, E., Couté, B., Jeannot, M., & Levasseur-Regourd, A. C. Wavelength dependence of linear polarization in the visible and near infrared domain for large levitating grains (PROGRA2 instruments). *J. Quant. Spectrosc. Radiat. Transf.*, *146*, 424–430. https://doi.org/10.1016/j.jqsrt.2014.02.024, 2014.

Renard, J.-B., Francis, M., Hadamcik, E., Daugeron, D., Couté, B., Gaubicher, B., & Jeannot, M. Scattering properties of sands. 2. Results for sands from different origins. *App. Opt.*, *40*(18), 3352–3559. http://www.icare.univ-lille1.fr/progra2/, 2010.

Renard, J.-B., Hadamcik, E., Worms, J.-C., & Hadamcik, E. The laboratory PROGRA2 database to interpret the linear polarization and brightness phase curves of light scattered by solid particles in clouds and layers. *J. Quant. Spectrosc. Radiat. Transf.*, *320*, 108980. https://doi.org/10.1016/j.jqsrt.2024.108980ï, 2024.

Rodríguez, S., & López-Darias, J. Extreme Saharan dust events expand northward over the Atlantic and Europe, prompting record-breaking PM $_{10}$ and PM $_{2.5}$ episodes. *Atmos. Chem. Phys.*, *24*(20), 12031–12053. https://doi.org/10.5194/acp-24-12031-2024, 2024.

Rodríguez, S., Querol, X., Alastuey, A., Kallos, G., & Kakaliagou, O. Saharan dust contributions to PM10 and TSP levels in Southern and Eastern Spain. *Atmos. Environ.*, *35*(14), 2433–2447. https://doi.org/10.1016/S1352-2310(00)00496-9, 2001.

Rosenfeld, D., Andreae, M. O., Asmi, A., Chin, M., de Leeuw, G., Donovan, D. P., Kahn, R., Kinne, S., Kivekäs, N., Kulmala, M., Lau, W., Schmidt, K. S., Suni, T., Wagner, T., Wild, M., & Quaas, J. Global observations of aerosol-cloud-precipitation-climate interactions. *Rev. Geophys.*, *52*(4), 750–808. https://doi.org/10.1002/2013RG000441, 2014.

Saito, M., and Yang, P. Advanced bulk optical models linking the backscattering and microphysical properties of mineral dust, *Geophys. Res. Lett.*, *48*, e2021GL095121. https://doi.org/10.1029/2021GL095121, 2021.

Saito, M., Yang, P., Ding, J., and Liu, X. A comprehensive database of the optical properties of irregular aerosol particles for radiative transfer simulations. *J. Atmos. Sci.*, *78*, 2089-2111. https://doi.org/10.1175/JAS-D-20-0338.1, 2021.

Saito, M., & Yang, P. Quantifying the impact of the surface roughness of hexagonal ice crystals on backscattering properties for lidar-based remote sensing applications. *Geophys. Res. Lett.*, 50, e2023GL104175. https://doi.org/10.1029/2023GL104175, 2023.

Sakai, T., Nagai, T., Zaizen, Y., & Mano, Y. Backscattering linear depolarization ratio measurements of mineral, sea-salt, and ammonium sulfate particles simulated in a laboratory chamber. *App. Opt.* *49*(23), 4441-4449. https://doi.org/10.1364/AO.49.004441, 2010.

Salvador, P., Alonso-Pérez, S., Pey, J., Artíñano, B., de Bustos, J. J., Alastuey, A., & Querol, X. African dust outbreaks over the western Mediterranean Basin: 11-year characterization of atmospheric circulation patterns and dust source areas. *Atmos. Chem. Phys.*, *14*(13), 6759–6775. https://doi.org/10.5194/acp-14-6759-2014, 2014.

Schmeisser, L., Andrews, E., Ogren, J. A., Sheridan, P., Jefferson, A., Sharma, S., Kim, J. E., Sherman, J. P., Sorribas, M., Kalapov, I., Arsov, T., Angelov, C., Mayol-Bracero, O. L., Labuschagne, C., Kim, S. W., Hoffer, A., Lin, N. H., Chia, H. P., Bergin, M., … Wu, H. Classifying aerosol type using in situ surface spectral aerosol optical properties. *Atmos. Chem. Phys.*, *17*(19), 12097–12120. https://doi.org/10.5194/acp-17-12097-2017, 2017.

Titos, G., del Águila, A., Cazorla, A., Lyamani, H., Casquero-Vera, J. A., Colombi, C., Cuccia, E., Gianelle, V., Močnik, G., Alastuey, A., Olmo, F. J., & Alados-Arboledas, L. Spatial and temporal variability of carbonaceous aerosols: Assessing the impact of biomass burning in the urban environment. *Sci. Tot. Environ.*, *578*, 613–625. https://doi.org/https://doi.org/10.1016/j.scitotenv.2016.11.007, 2017.

Titos, G., Lyamani, H., Pandolfi, M., Alastuey, A., & Arboledas, L. Identification of fine (PM 1) and coarse (PM 10-1) sources of particulate matter in an urban environment. *Atmos. Environ.*, *89*, 593–602. https://doi.org/10.1016/j.atmosenv.2014.03.001, 2014.

Torres, B., Dubovik, O., Fuertes, D., Schuster, G., Eugenia Cachorro, V., Lapyonok, T., Goloub, P., Blarel, L., Barreto, A., Mallet, M., Toledano, C., & Tanré, D. Advanced characterisation of aerosol size properties from measurements of spectral optical depth using the GRASP algorithm. *Atmos. Meas. Tech.*, *10*(10), 3743–3781. https://doi.org/10.5194/amt-10-3743-2017, 2017.

Valenzuela, A., Olmo, F. J., Lyamani, H., Antón, M., Quirantes, A., & Alados-Arboledas, L. Aerosol radiative forcing during African desert dust events (2005–2010) over Southeastern Spain. *Atmos. Chem. Phys.*, *12*(21), 10331–10351. https://doi.org/10.5194/acp-12-10331-2012, 2012a.

Valenzuela, A., Olmo, F. J., Lyamani, H., Antón, M., Quirantes, A., & Alados-Arboledas, L. Classification of aerosol radiative properties during African desert dust intrusions over southeastern Spain by sector origins and cluster analysis. *J. Geophys. Res. Atmos.*, *117*(D6). https://doi.org/https://doi.org/10.1029/2011JD016885, 2012b.

Valenzuela, A., Olmo, F. J., Lyamani, H., Antón, M., Titos, G., Cazorla, A., & Alados-Arboledas, L. Aerosol scattering and absorption Angström exponents as indicators of dust and dust-free days over Granada (Spain). *Atmos. Res.*, *154*, 1–13. https://doi.org/10.1016/j.atmosres.2014.10.015, 2015.

Valenzuela, A., Olmo, F. J., Lyamani, H., Granados-Muñoz, M. J., Antón, M., Guerrero-Rascado, J. L., Quirantes, A., Toledano, C., Perez-Ramírez, D., & Alados-Arboledas, L. Aerosol transport over the western mediterranean basin: Evidence of the contribution of fine particles to desert dust plumes over alborán island. *J. of Geophys. Res.*, *119*(22), 14,028-14,044. https://doi.org/10.1002/2014JD022044, 2014.

Volten, H., Muñoz, O., Rol, E., De Haan, J. F., Vassen, W., Hovenier, J. W., Muinonen, K., & Nousiainen, T. Scattering matrices of mineral aerosol particles at 441.6 nm and 632.8 nm. *J. Geophys. Res. Atmos.*, *106*(D15), 17375–17401. https://doi.org/10.1029/2001JD900068, 2001.

West, R. A., Doose, L. R., Eibl, A. M., Tomasko, M. G., & Mishchenko, M. I. Laboratory measurements of mineral dust scattering phase function and linear polarization. *J. Geophys. Res. Atmos.*, *102*(14), 16871–16881. https://doi.org/10.1029/96jd02584, 1997.

Wyatt, P. J., Schehrer, K. L., Phillips, S. D., Jackson, C., Chang, Y.-J., Parker, R. G., Phillips, D. T., & Bottiger, J. R. Aerosol particle analyzer. *App. Opt.*, *27*(2), 217–221. https://doi.org/10.1364/AO.27.000217, 1988.

Zhang, X., Dai, C., Wei, H., Liu, J., Li, W., Wu, K., & Zou, S. Optical properties of mineral dust aerosols with non-absorptive coating: A numerical investigation. *J. Quant. Spectrosc. Radiat. Transf.*, *302*, 108564. https://doi.org/10.1016/j.jqsrt.2023.108564, 2023.

Zhang, X., Wei, H., Zou, S., Duan, J., Li, W., & Dai, C. Effect of nitrate coatings on the optical properties of mineral dust particles during the haze aging process. *J. Quant. Spectrosc. Radiat. Transf.*, *277*, 107966. https://doi.org/10.1016/j.jqsrt.2021.107966, 2022.